Resonance conditions, detection quality, and single-molecule sensitivity in fluorescence-encoded infrared vibrational spectroscopy

Lukas Whaley-Mayda,[1] Abhirup Guha,[1] and Andrei Tokmakoff[1, a)]

Department of Chemistry, James Franck Institute, and Institute for Biophysical Dynamics, The University of Chicago, Chicago, Illinois 60637, USA

(Dated: 5 July 2022)

Fluorescence-encoded infrared (FEIR) spectroscopy is a vibrational spectroscopy technique that has recently demonstrated the capability of single-molecule sensitivity in solution without near-field enhancement. This work explores the practical experimental factors that are required for successful FEIR measurements in both the single-molecule and bulk regimes. We investigate the role of resonance conditions by performing measurements on a series of coumarin fluorophores of varying electronic transition frequencies. To analyze variations in signal strength and signal to background between molecules, we introduce an FEIR brightness metric that normalizes out measurement-specific parameters. We find that the effect of the resonance condition on FEIR brightness can be reasonably well described by the electronic absorption spectrum. We discuss strategies for optimizing detection quality and sensitivity in bulk and single-molecule experiments.

[a)]Author to whom correspondence should be addressed: tokmakoff@uchicago.edu

I. INTRODUCTION

Single-molecule (SM) vibrational spectroscopy has emerged as a powerful class of tools for investigating chemical phenomena. Probing vibrations offers sensitivity to chemical connectivity and bonding, intermolecular contacts, and other angstrom-scale changes in structure—the molecular properties and events that drive chemistry. Simultaneously, SM detection accesses the individual characteristics of molecules that would otherwise be lost in the ensemble average for heterogeneous systems. From a time-dependent perspective, SM observation can reveal the trajectory of a molecular observable as it freely explores its configurational space. Provided sufficient time-resolution and sampling, such trajectory measurements represent the purest form of studying kinetics and dynamics in that the residence times within, transitions between, and overall history of states visited are directly accessible. While this combination of capabilities offers enormous potential, SM vibrational detection presents unique technical challenges that compound the difficulty of experiments, and continues to be developed in many different forms.

The primary difficulties associated with the optical detection of molecular vibrations are their small cross-sections and fast non-radiative relaxation. Currently, the most prevalent approaches employ near-field optical effects to both amplify the light-matter interaction and reduce the observation volume to the point were SM detection is possible. The most important examples are surface- and tip-enhanced Raman spectroscopy (SERS and TERS) which achieve near-field signal enhancement through nanometer proximity or direct adsorption to a metallic nanostructure, and have been used extensively for SM spectroscopy for over two decades.[1–5] Infrared (IR) techniques based on scattering-type scanning near-field microscopy (IR s-SNOM), atomic force microscopy (AFM-IR), and other near-field schemes can isolate signals from small ensembles of oscillators at nanometer length scales,[6,7] and are being developed toward SM detection with some recent success.[8] Non-optical methods based on scanning tunnelling microscopy (STM) have also been used to probe the vibrations of individual molecules, and similarly rely on sub-nanometer localization with a metallic probe.[9] However, the necessity for contact with a surface, nanostructure, or probe imposes severe restrictions on the types of samples that can be studied with these methods. Critically, molecular systems in solution or other condensed-phase environments where these requirements are too perturbative remain out of reach.

An alternative approach that circumvents the optical near-field is to couple the ground-state vibrational spectroscopy to a fluorescence read-out signal that can be detected at the SM level

using the by now well-developed far-field microscopy methods of SM fluorescence spectroscopy. This idea long predates SM spectroscopy and was explored in the work of Laubereau, Seilmeier, and Kaiser, who introduced a double-resonance method employing a picosecond IR pulse followed by a picosecond UV/Vis pulse to resonantly excite vibrations and then selectively bring those molecules to their fluorescent electronic excited state.[10–13] Critical to this approach is the use of pulses that are of similar duration or shorter than the typically picosecond vibrational lifetimes. A similar double-resonance approach using stimulated Raman excitation instead of IR absorption was proposed by Wright,[14] and later explored theoretically by Orrit and co-workers as a potential technique for SM vibrational detection.[15] Min and coworkers successfully established this double-resonance Raman method—stimulated Raman excited fluorescence (SREF) spectroscopy—demonstrating SM vibrational detection operating entirely in the far-field.[16,17] Our group has built upon the original IR-pumped method, fluorescence-encoded IR (FEIR) spectroscopy, employing femtosecond pulses to perform ultrafast Fourier transform spectroscopy,[18–20] and recently showed that SM sensitivity can be achieved in solution.[21]

While our initial demonstration of SM sensitivity is encouraging, developing FEIR spectroscopy as a generally useful method will require a more thorough understanding of the optical and molecular factors involved in SM FEIR detection. Specifically, what makes a molecule a good FEIR chromophore, and given such a molecule, how is FEIR detection optimized? This first question can be initially addressed by considering the minimum requirements of a good, i.e. SM capable, FEIR chromophore from a heuristic standpoint: high fluorescence brightness, strong IR activity of the target vibration(s), and strong vibronic coupling of this target vibration to the electronic transition, e.g. Franck-Condon activity. Next, the double-resonance condition must be met: the IR frequency ω_{IR} is tuned to cover the vibrational transition while the visible frequency ω_{vis} should "make up the difference" to bring the molecule to the electronic excited state, i.e.

$$\omega_{\mathrm{IR}} + \omega_{\mathrm{vis}} = \omega_{eg}, \tag{1}$$

where ω_{eg} is the electronic transition frequency. Practically speaking, this relation suggests that the visible pulse should be pre-resonant with the electronic absorption band by an amount commensurate with the target vibrational frequency. However, given the typically broad electronic lineshape in room-temperature solution with its interplay of intramolecular vibrational and solvation contributions, it is not *a priori* clear where this optimal resonance is located, or even to what extent the equilibrium absorption lineshape is a useful or predictive guide. Furthermore, direct excitation by

the visible pulse produces an undesirable fluorescence background that degrades detection contrast and therefore must also be considered in the optimization of the resonance condition.

Motivated by these questions, in this paper we investigate the practical experimental factors that govern FEIR signal strength and detection quality with the objective of elucidating the requirements for achieving SM sensitivity. We introduce an experimental FEIR brightness metric that accounts for instrumental parameters to isolate the intrinsic molecular factors that control signal size, and thereby facilitates comparison between different chromophores. We will focus on the particular role of the resonance condition in optimizing FEIR brightness and signal to noise. Perhaps the most direct experiment to capture the effect of electronic resonance would be to excite a single vibration at fixed ω_{IR} while tuning ω_{vis}. However, our current instrument is limited to a fixed ω_{vis}, so here we adopt the strategy of performing measurements across a series of dyes whose electronic spectra span a range of different frequencies. Motivated by our demonstration of SM sensitivity for coumarin 6 (C6) in acetonitrile-d3, we use a set of structurally-similar coumarin dyes in the same solvent in order to keep the vibrational and vibronic aspects of the chromophores as similar as possible. Clearly these vibration-specific factors are crucial for sensitive FEIR detection, and we will address mode-specific considerations including normal mode character and molecular symmetry with the aid of more detailed theory and electronic structure calculations in a subsequent publication.

Questions of signal strength, detection sensitivity, and 'goodness' of chromophore are also fundamentally coupled to the spectroscopic information content of an experiment. As a nonlinear ultrafast technique, FEIR spectroscopy can be used to access information beyond linear vibrational spectra, including relaxation dynamics, relative orientation of the vibrational and electronic transition dipoles, and inter-mode coherence and dephasing. However, our analysis here is concerned with experimental photon count rates and signal to noise at a practical level. We find that the electronic absorption spectrum can predict the dependence of FEIR brightness on the resonance condition to a reasonable degree across the full frequency range considered. For bulk measurements, signal to noise is limited by background fluorescence from direct visible excitation, and therefore detuning from resonance to decrease the overlap of ω_{vis} with the tail of the electronic band is often desirable. However, at SM equivalent concentrations background is mostly of non-molecular origin and maximal resonance should be employed. We observe saturation of the vibronic encoding transition by the visible pulse, which ultimately limits the upper range of molecular emission rates that can be achieved.

II. EXPERIMENTAL METHODS

A. Steady-state spectroscopic characterization of coumarin FEIR dyes

Ten commercially available 7-aminocoumarin dyes were obtained from Sigma (C30 and C153), TCI America (C314, C337, C334, and C7), Acros Organics (C343 and C6), and Exciton-Luxottica (C525 and C545), and used as received. For each Coumarin dye, Fourier transform IR (FTIR) absorption measurements were performed in 1-5 mM acetonitrile-d3 solution at 100-500 μm pathlength using a Bruker Tensor 27 FTIR spectrometer at 2 cm^{-1} resolution. Each FTIR spectrum was solvent-subtracted and converted to molar extinction units by dividing the measured absorbance by concentration and pathlength.

UV/Vis absorption was performed with an Agilent Technologies Cary 5000 spectrophotometer using a 4 nm excitation bandwidth with 0.5 nm steps. Dye solutions in acetonitrile at 40 μM were measured in a 1 cm pathlength quartz cuvette, resulting in maximum absorbances < 2, which was determined to be within the linear range of the spectrometer. Each spectrum was corrected by an independently measured solvent blank and converted to molar extinction units. An exponential fit to the low-frequency absorption wing was used to extract the extinction value at ω_{vis} for all coumarins but C545 (Figure S1 in the supplementary material).

Fluorescence spectra were measured with a Horiba Flouorlog-3 fluorimeter using right-angle collection from 1 cm pathlength quartz cuvettes. The concentration was adjusted (typically < 2 μM) to keep the maximum absorbance below 0.1 to avoid inner filter artifacts. Excitation-emission surfaces were measured with 3 nm slit widths for both excitation and emission monochromators. The excitation spectra acquired by integrating over the emission axis were found to match the lineshape of the UV/Vis absorption, and fluorescence emission spectra were acquired by integrating over the excitation axis. Fluorescence quantum yields were measured relative to coumarin 153 in ethanol (ϕ= 0.53) as a standard using the procedure outlined in Ref.22, and we estimate uncertainties of $\sim$10% for these values. All solutions were air-saturated.

B. FEIR measurements

FEIR measurements were performed with the experimental apparatus described previously.[20,21] Briefly, 230 fs IR pulses (center-frequency ω_{IR} = 1620 cm^{-1}, 120 cm^{-1} fwhm bandwidth) were generated with a home-built OPA pumped by a 1 MHz repetition-rate Yb fiber laser (Coherent

Monaco).[23] These pulses were sent through a Mach-Zehnder interferometer to create a collinear pulse-pair with controllable delay τ_{IR}, then focused into the sample from below using a ZnSe aspheric lens of numerical aperture (NA) ∼0.7. The visible encoding pulse (∼330 fs, center-frequency ω_{vis} = 19360 cm^{-1} (= 516.5 nm), fwhm bandwidth < 80 cm^{-1} (< 2 nm)) was generated by frequency doubling the fiber laser fundamental, delayed with respect to the stationary pulse of the IR pulse-pair by τ_{enc}, and focused into the sample from above, collinear to the IR, with a 0.8 NA air objective. The IR and visible pulses were linearly polarized with parallel orientation in the sample. Fluorescence was collected with the same objective, separated geometrically from the visible excitation beam by a long-pass dichroic, sent through both a ω_{vis}-band rejection and selective fluorescence bandpass filter, and imaged onto a single-photon counting avalanche photodiode (SPAD) using its 50 μm diameter active area as a confocal aperture to remove out of focus light. Considering the NA and magnification (57×), the radius of this aperture corresponds to 4.2 optical units at ω_{vis}, or equivalently ∼1.1 times the Airy disk radius. While slightly larger than the optimal size for maximum signal to noise in confocal microscopy (2.4-3.3 optical units), this aperture is close to that for producing optimal signal to noise in fluorescence correlation spectroscopy (∼4.5 optical units).[24–26]

Sample solutions (30-100 μM in acetonitrile-d3) were held between a 1 mm thick CaF_2 window (bottom, IR side) and either a 175 μm-thick glass or 150 μm-thick CaF_2 coverslip (top, visible side), separated by a 50 μm PTFE spacer, and positioned so that the visible confocal volume was ∼20 μm below the coverslip. Detrimental thermal effects due to IR absorption by the conventional glass coverslips limited the upper range of IR power that could be used and reduced signal levels.[20] However, switching to the CaF_2 coverslips effectively removed these artifacts, yielding FEIR signals ∼3 times larger. In this work, both types of coverslips were used (glass for the data in Section IV C, CaF_2 in Section IV D), however quantitative comparisons are only made among measurements using the same type.

The IR pulse energy at the sample during total constructive interference between the pulse-pair (τ_{IR} = 0) was kept constant at ∼50 nJ, although variations of ±5% occurred between measurements. Considering the pulse duration and $1/e^2$ focal radius of ∼9 μm, the corresponding peak intensity is ∼160 GW/cm^2, with a pulse-train average intensity of ∼40 kW/cm^2. The visible pulse energy was varied between 10 fJ – 100 pJ depending on the concentration and resonance condition for each sample, which considering pulse duration and 0.34 μm $1/e^2$ focal radius corresponds to peak intensities of 0.015-150 GW/cm^2, or average intensities of 0.005-50 kW/cm^2. In each case

the visible pulse energy was chosen to keep the total fluorescence count rate from exceeding 200 kHz (20% of repetition rate) to prevent pile-up distortions—caused by the arrival of multiple photons at the detector per excitation cycle, only the first of which can be registered—from being too severe (< 10% error). The raw count rates were then corrected for pile-up using the relation $x_{corrected} = -r\ln(1 - x_{raw}/r)$ where $r = 994.7$ kHz is the exact repetition-rate (details provided in Section 2 of the supplementary material).

III. THEORETICAL PRINCIPLES OF SIGNAL AND BACKGROUND SIZE

The total photon count rate F_{tot} (Hz) detected in an FEIR measurement consists of the following components

$$F_{\mathrm{tot}}(\tau_{\mathrm{IR}}, \tau_{\mathrm{enc}}) = F(\tau_{\mathrm{IR}}, \tau_{\mathrm{enc}}) + F_0 + B. \tag{2}$$

Here F is the desired FEIR signal which depends on the pulse delays, F_0 is a constant background fluorescence due to direct excitation of the target molecule by the visible pulse alone, and B encapsulates all other sources of background not arising from the target molecule, e.g. solvent Raman scattering, emission from impurities and optics, and detector dark counts. For the sake of this analysis we will consider the IR pulse-pair delay fixed at $\tau_{\mathrm{IR}} = 0$, i.e. 2-pulse experiments (one IR and one visible pulse). Previously we have referred to such experiments as 1-pulse,[20] or 1-IR-pulse measurements,[21] however here we modify our terminology to reflect the total number of pulses. The 2-pulse amplitude $F(\tau_{\mathrm{enc}})$ reflects the integrated response of all vibrations within the bandwidth of the IR pulse spectrum. The fractional contribution to the count rate from a distinct vibrational resonance can in principle then be calculated using the FEIR spectrum measured at that encoding delay, although we will not explore this strategy here. We will consider early, positive τ_{enc} where F is near its maximum, and suppress the time argument for brevity. In general, successful FEIR detection requires the ability to distinguish the signal F against the background $F_0 + B$, and therefore a practical figure of merit is the modulation ratio

$$M = \frac{F}{F_0 + B}, \tag{3}$$

i.e. the ratio of useful FEIR photons to all other detected photons. The presence of F_0—a fluorescence signal from the target molecule, yet contributing to the background—is an important aspect of the practical optimization of FEIR detection. As a signal to background ratio, M is a readily apparent feature of the raw data, and consequently a convenient target for optimization. However,

the more fundamental descriptor of detection quality is the signal to noise ratio

$$\mathrm{SNR} = \frac{FT}{\sqrt{F_{\mathrm{tot}}T}} = \frac{F}{\sqrt{F+F_0+B}}\sqrt{T} \tag{4}$$

defined here for the shot noise limit as the ratio of the number of FEIR photons accumulated during the integration time T relative to the Poisson noise of the total number of detected photons. Therefore, both the contrast M and the absolute magnitude of the signal F need to be considered to maximize the SNR.

A. FEIR Brightness

Since the absolute size of an FEIR signal is ultimately governed by the molecular emission rate, we seek to relate experimental count rates to the overall probability of excitation, emission, and detection per molecule. Furthermore, accounting for the instrument-specific factors that influence these probabilities should in principle isolate purely molecular metrics that describe the propensity of a given vibration to be detected via FEIR. In conventional fluorescence spectroscopy, such a metric is the fluorescence brightness, which characterizes a fluorophore's ability to emit a photon in response to optical excitation. From an external spectroscopic standpoint, brightness can be defined as the product of absorption cross-section (at the excitation frequency) and fluorescence quantum yield ($\sigma_{\mathrm{el}} \times \phi$).[22,27,28] Alternatively, fluorescence brightness has also been defined directly from experimental SM count rates, which can be related to $\sigma_{\mathrm{el}} \times \phi$ with knowledge of the excitation beam photon flux and overall detection efficiency.[29] This concordance of definitions is made possible by the linear nature of the fluorescence excitation process, which facilitates a straightforward separation of molecular and optical factors.

In contrast, FEIR excitation is a nonlinear process consisting of IR excitation of the vibrational $v = 1$ population followed sequentially by a vibronic transition to the excited electronic state (Figure 1). To a first approximation, these two steps may each be considered as the resonant absorption of one photon (IR, then visible), producing a linear dependence separately in the intensity of the IR and visible fields. Importantly, this process is distinct from two-photon absorption, where there is typically no resonant intermediate state and the transition must occur instantaneously, i.e. within the temporal profiles of the pulses. The overall FEIR excitation process competes with picosecond vibrational relaxation, and its efficiency is therefore sensitive to aspects of the temporal pulse profiles beyond peak or integrated photon fluxes. Additionally, multimode effects like the coherent excitation of pairs of vibrational fundamentals within the IR bandwidth further complicate the

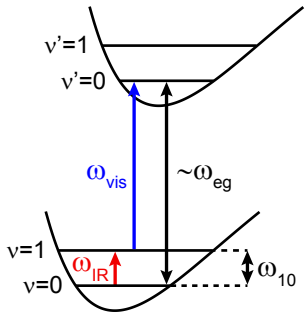

FIG. 1. Energy-level diagram for FEIR excitation of a single vibration coupled to the electronic transition.

interplay between molecular and optical factors.[19] These effects can be properly incorporated into a theoretical description of FEIR excitation based on time-domain response functions for the electronic excited population to 4$^{\text{th}}$-order in the incident field, but are beyond the scope of the current discussion.

Given these theoretical complexities, here we take a practical route to defining FEIR brightness based on experimental count rates and a simple phenomenological model for how the signal scales with experimental parameters. We assume the overall probability P_{ex} that a molecule is electronically excited in response to a pulse sequence follows the bilinear intensity dependence

$$P_{\text{ex}} = aI_{\text{IR}}I_{\text{vis}} \tag{5}$$

where I_{IR} and I_{vis} are peak pulse intensities (GW cm^{-2}) and a plays the role of an FEIR cross-section and is defined by this relation. While neglecting time-dependence and pulse duration effects in general, this relation is applicable to varying the energy of pulses with fixed time-delays and temporal profiles. The measured count rate is proportional to P_{ex}, specifically

$$F = r\langle N\rangle \eta \phi a I_{\text{IR}} I_{\text{vis}}, \tag{6}$$

where r is the pulse repetition-rate, $\langle N\rangle$ is the average number of molecules in the probe volume, η is the overall photon detection efficiency, and ϕ the fluorescence quantum yield.[30] We have previously verified this linear I_{IR}- and I_{vis}-dependence for bulk samples where $P_{\text{ex}} \ll 1$ for any given molecule.[20] In analogy to fluorescence brightness, the FEIR brightness in the context of this model is $a \times \phi$.

Our approach is to extract this value, or a proportional quantity, from the measured count rate

by dividing out the experimental and instrument-specific parameters in Eq. (6). Not all of these parameters can be directly measured, although reasonable estimates can be made. For example, the detection efficiency can be approximated as

$$\eta = \eta_{\text{coll}} \int s_{\text{fl}}(\omega) T_{\text{bp}}(\omega) \eta_{\text{detector}}(\omega) d\omega. \tag{7}$$

Here η_{coll} is the geometric collection efficiency of the objective lens and optical path coupling the photon onto the detector, which can depend on the specific details of the experimental configuration in complicated ways and is difficult to measure absolutely. The objective's numerical aperture (NA) is the dominant factor, and for isotropic emission in a homogeneous medium of refractive index n the objective's collection efficiency is $\sin^2\left(\frac{1}{2}\sin^{-1}(\text{NA}/n)\right)$, which is 10% in our experiments. The frequency integral in Eq. (7) is the overlap of the molecule's area-normalized fluorescence spectrum $s_{\text{fl}}(\omega)$, transmission function of the emission filters' bandpass $T_{\text{bp}}(\omega)$, and detector quantum efficiency $\eta_{\text{detector}}(\omega)$. For our detector $\eta_{\text{detector}}(\omega)$ is $\sim$45% and slowly varying over the emission frequencies considered.[31] The factor that is significantly variable between different molecules is the fraction of the fluorescence spectrum transmitted by the bandpass filters

$$\eta_{\text{bp}} = \int s_{\text{fl}}(\omega) T_{\text{bp}}(\omega) d\omega, \tag{8}$$

which may be calculated directly from steady-state fluorescence and transmission measurements. Overall, using these estimates $\eta \approx 0.045 \times \eta_{\text{bp}}$, although this is likely only an upper bound due to further unknown factors in η_{coll}.

Similarly, $\langle N \rangle$ is difficult to measure in general, but can be represented up to proportionality by the solution concentration C (mol L^{-1}). Previously we have measured $\langle N \rangle$ directly from nM solutions of C6 by performing FEIR correlation spectroscopy (FEIR-CS), finding $\sim$0.65 molecules/nM, or, assuming this relation is scalable to any concentration $\langle N \rangle = 0.65 \times 10^{-9} C$.[21] However, to ensure we only use parameters that are directly controlled or measured, we define FEIR brightness (mol^{-1} L GW^{-2} cm^4) as

$$q = \frac{F}{rC\eta_{\text{bp}} I_{\text{IR}} I_{\text{vis}}} \approx 1.44 \times 10^{12}\,(\text{mol}^{-1}\text{L})\,\phi a \tag{9}$$

where the second approximate equality uses the estimates stated above to isolate the fully-corrected FEIR brightness in Eq. (6).

B. FEIR cross-section

The FEIR cross-section a reflects the microscopic molecular factors governing the overall excitation process, shown in Figure 1. While a complete description that includes the effects of vibrational relaxation, pulse durations and spectra, and multimode excitation is best handled by a response function calculation, here we discuss the relevant quantities from a heuristic standpoint. For a single vibration within the Condon approximation, and assuming early encoding delays where vibrational relaxation is negligible

$$a \sim |\mu_{eg}|^2 |\langle 1_g | 0_e \rangle|^2 |\mu_{10}|^2 \cdot Y \cdot \Delta(\omega_{\text{vis}} - (\omega_{eg} - \omega_{10})). \tag{10}$$

Here ω_{10} and μ_{10} are the vibrational frequency and transition dipole moment, ω_{eg} and μ_{eg} are the pure electronic transition frequency and dipole moment, and $\langle 1_g | 0_e \rangle$ is the Franck-Condon factor describing the vibrational-electronic coupling. $Y = \langle [\hat{\mu}_{eg} \cdot \hat{\varepsilon}_{\text{vis}}]^2 [\hat{\mu}_{10} \cdot \hat{\varepsilon}_{\text{IR}}]^2 \rangle$ is an orientational factor determined by the projection of the pulse polarization vectors $\hat{\varepsilon}_{\text{IR}}$ and $\hat{\varepsilon}_{\text{vis}}$ onto the transition dipole directions $\hat{\mu}_{10}$ and $\hat{\mu}_{eg}$, averaged over the orientational distribution present in the experiment. Such orientational factors are common to coherent 3$^{\text{rd}}$-order nonlinear techniques, the most directly analogous being 2D-VE spectroscopy,[32,33] however in terms of overall magnitude this factor plays a minor role, and we will not discuss its contribution in detail here. The final factor $\Delta(\omega_{\text{vis}} - (\omega_{eg} - \omega_{10}))$ is a normalized resonance term that accounts for the spectral overlap of the visible pulse with the encoding transition, i.e. the vibronic transition from the $v = 1$ state of the vibration being pumped to the excited electronic manifold. Here we have assumed that the IR pulse is spectrally broad compared to the vibrational transition and tuned to resonance $\omega_{\text{IR}} \approx \omega_{10}$, so that Δ describes the detuning from the resonance condition in Eq. (1). As an effective lineshape function for the encoding transition, Δ should in principle be influenced by many of the same intramolecular vibrational and solvation coordinates that govern the lineshape of the equilibrium electronic transition.

C. Background

In analogy to Eq. (6), the directly excited fluorescence background F_0 can be written as

$$F_0 = r\langle N \rangle \eta \phi a_0 I_{\text{vis}}, \tag{11}$$

where a_0 is the coefficient relating the probability of one-photon electronic excitation to the visible peak pulse intensity. Specifically, a_0 is related to the absorption cross-section and visible pulse duration t_{vis} as $a_0 = \sigma_{\mathrm{el}}(\omega_{vis})t_{\mathrm{vis}}/\hbar\omega_{vis}$. Higher-order contributions in I_{vis}, e.g. two-photon absorption, can also become significant in cases when ω_{vis} is sufficiently off-resonance from the electronic absorption band. We define the direct excitation brightness ($\mathrm{mol^{-1}\ L\ GW^{-1}\ cm^2}$) as

$$q_0 = \frac{F_0}{rC\eta_{\mathrm{bp}}I_{\mathrm{vis}}}. \tag{12}$$

When linear absorption is the dominant contribution, $q_0 \propto \phi a_0$ with the same estimated proportionality factor as Eq. (9), and represents the conventional fluorescence brightness excited at ω_{vis}. The nonlinearity of the FEIR excitation process spatially localizes signal generation to the product of the IR and visible intensity profiles. However, because the size of the IR focus is at least an order of magnitude larger than the visible, the spatial distribution of FEIR signal generation within the 50 μm-thick solution layer is essentially the same as the one-photon fluorescence background, which precludes the use of more aggressive confocal filtering to selectively suppress F_0.

The sources of background not originating from the target molecule can be numerous, and naturally become increasingly prevalent in the low concentration regime of SM experiments. However, these contributions to the non-molecular background B can be decomposed by its excitation power dependence

$$B = d + bI_{\mathrm{vis}} + \cdots \tag{13}$$

The constant d represents the detector dark count rate ($\sim$40 Hz in our experiments), while the term linear in I_{vis} describes Raman scattering from the solvent as a well as fluorescence from the optics or undesired impurities. In principle, higher-order terms like multiphoton-excited fluorescence could contribute but do not appear to be important under our experimental conditions. We have not observed any background signal due to excitation with the IR pulse alone.

IV. RESULTS AND DISCUSSION

A. Electronic absorption and fluorescence spectra

The series of 10 coumarin dyes used in this study is shown in Figure 2(a). Our naming convention follows the Kodak catalogue, with the exception of C525 and C545 which are Exciton catalogue names.[34] The electronic spectroscopy of the $S_0 \rightarrow S_1$ transition is influenced by the

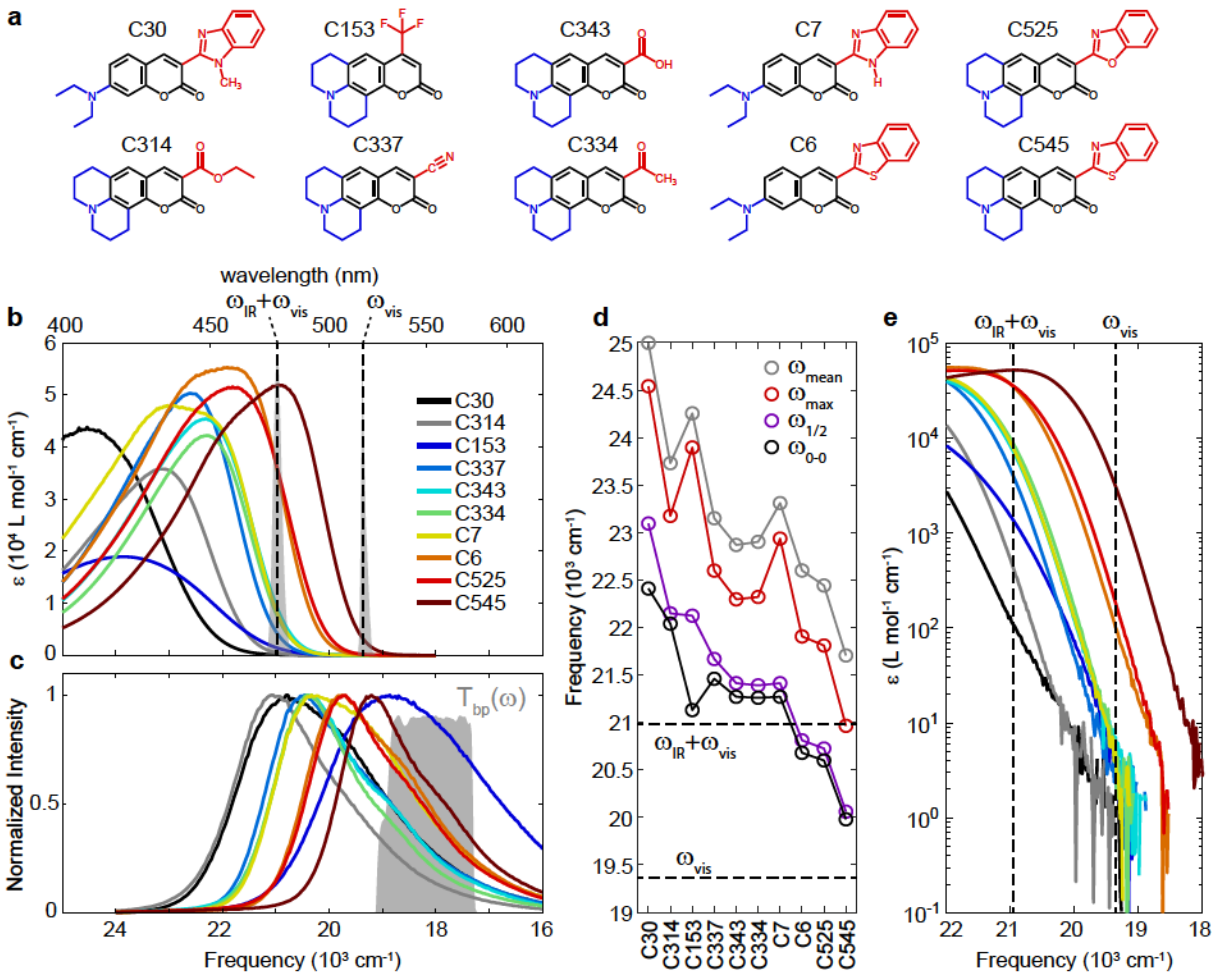

FIG. 2. Electronic absorption and emission characteristics of the coumarin dye series in acetonitrile. (a) Structures of the coumarin dyes with their abbreviated names. (b) Electronic absorption spectra plotted as molar decadic extinction on a linear wavenumber scale (lower x-axis common with (c)) with corresponding wavelength values on the upper x-axis. Visible pulse spectrum (gray) with center frequency (dashed black) ω_{vis} indicated, and similarly for the IR/vis spectral convolution (center frequency $\omega_{\mathrm{IR}} + \omega_{\mathrm{vis}} = 20980$ cm^{-1} = 477 nm). (c) Normalized fluorescence spectra with the emission bandpass $T_{\mathrm{bp}}(\omega)$ shown in gray. (d) First moment of the absorption spectrum (ω_{mean}), frequency of the absorption maximum (ω_{max}), half-way point up the low-frequency edge ($\omega_{1/2}$), and 0-0 transition (ω_{0-0}, see text) for each coumarin. (e) Low-frequency edges of the electronic absorption spectra in (b) plotted on a logarithmic y-axis. In (d) and (e) ω_{vis} and $\omega_{\mathrm{IR}} + \omega_{\mathrm{vis}}$ are indicated by dashed lines.

charge-transfer character of the S_1 excited state, which is modulated by the electron-donating and electron-withdrawing abilities of the amino group (shown in blue) and substituent on the lactone

ring (shown in red), respectively.[35–37] The variation of electron-withdrawing group and degree of alkylation of the amino group consequently tunes the absorption and fluorescence spectra (Figures 2(b) and (c), respectively) across a frequency range of $\sim$3000 cm^{-1}. We illustrate the resulting span of FEIR excitation resonance conditions by overlaying the visible pulse spectrum and convolution of visible and IR pulse spectra on the absorption bands in Figure 2(b) (spectral distributions shown in gray, with respective center frequencies ω_{vis} and $\omega_{\text{IR}} + \omega_{\text{vis}}$ denoted by dashed lines). The IR/visible spectral convolution, formally the distribution of all IR + visible frequency sums accessible between their bandwidths, nominally indicates the breadth of double resonance around $\omega_{\text{IR}} + \omega_{\text{vis}}$ that can be supported by the pulse spectra, and has a fwhm of $\sim$140 cm^{-1}. Notably, both this distribution and the visible pulse spectrum are narrowband with respect to the coumarins' electronic absorption lineshapes. Figure 2(d) shows ω_{vis} and $\omega_{\text{IR}} + \omega_{\text{vis}}$ against various metrics characterizing the electronic absorption frequency (see also Table I): ω_{mean}, first moment of the band, ω_{max}, frequency of the band maximum, $\omega_{1/2}$, frequency of the half-way point up the low-frequency edge, and ω_{0-0}, an approximation of the 0-0 transition frequency given by the crossing point of the normalized absorption and fluorescence lineshapes. The coumarins have been ordered by decreasing $\omega_{1/2}$ values. For C30, the most blue-shifted coumarin under consideration, $\omega_{\text{IR}} + \omega_{\text{vis}}$ falls $\sim$1500 cm^{-1} below ω_{0-0}, while the three reddest—C6, C525, and C545—have $\omega_{\text{IR}} + \omega_{\text{vis}} > \omega_{0-0}$, notably with $\omega_{\text{IR}} + \omega_{\text{vis}} \approx \omega_{\text{max}}$ for C545.

While each of these electronic frequency metrics is influenced to some degree by the band's shape, they nevertheless cannot adequately account for the breadth of the lineshape. As a potentially more direct characterization of FEIR resonance, we will investigate $\varepsilon_{\text{el}}(\omega_{\text{IR}} + \omega_{\text{vis}})$—the value of the extinction coefficient at the double-resonance frequency. Figure 2(e) shows the same absorption spectra on a logarithmic y-axis to better show the extent of the low-frequency edge, with $\omega_{\text{IR}} + \omega_{\text{vis}}$ and ω_{vis} indicated by dashed lines. From the bluest to reddest coumarins in the series, $\varepsilon_{\text{el}}(\omega_{\text{IR}} + \omega_{\text{vis}})$ spans nearly 3 orders of magnitude. In principle this metric describes both detuning, through position on the lineshape, as well as electronic transition strength, through the extinction magnitude. Maximum extinction values, as well as oscillator strengths calculated from the molar decadic extinction spectra via the numerical relation $f = 4.32 \times 10^{-9} \int \varepsilon(\omega) d\omega$ with ω expressed in cm^{-1},[38,39] are listed in Table I and vary by a factor $\sim$3 across the series. In the context of the heuristic expression for FEIR cross-section in Eq. (10), $\varepsilon_{\text{el}}(\omega_{\text{IR}} + \omega_{\text{vis}})$ should supply information on $|\mu_{eg}|^2$ by proportionality with f, while we would also expect similarities with the ω_{vis}-dependence of the encoding lineshape function Δ in the presence of shared line-broadening

TABLE I. $S_0 \rightarrow S_1$ spectroscopic parameters of the coumarin dye series.

coumarin	ε_{max} (L mol^{-1} cm^{-1})	f[a]	ω_{max} (cm^{-1})	ω_{0-0} (cm^{-1})	$\Delta\omega_{edge}$[b] (cm^{-1})	Stokes shift[c] (cm^{-1})	ϕ	η_{bp}
30	43000	0.74	24500	22420	1240	3730	0.64	0.15
314	36000	0.47	23200	22000	900	2120	0.70	0.10
153	19000	0.36	23900	21200	1470	5030	0.65	0.35
337	50000	0.63	22600	21500	880	2130	0.76	0.18
343	42000	0.51	22300	21300	810	1960	0.63	0.18
334	45000	0.58	22300	21300	840	1920	0.89	0.16
7	48000	0.78	22900	21300	740	2600	0.86	0.23
6	55000	0.85	21900	20700	720	2150	0.89	0.29
525	51000	0.75	21800	20600	820	2120	0.75	0.28
545	52000	0.72	21000	20000	770	1750	0.71	0.39

[a] oscillator strength

[b] hwhm of a Gaussian fit to the red-edge of the absorption band

[c] Defined as the difference between the absorption and fluorescence band maxima

mechanisms.

Linear absorption of the visible pulse is controlled by $\varepsilon(\omega_{vis})$, which also varies dramatically by over 3 orders of magnitude across the coumarin series. Below a few percent of the band maxima, the low-frequency absorption tails exhibit an exponential frequency dependence, apparent as linear slopes in the logarithmic scaling of Figures 2(e) (exponential fits shown in Figure S1 and S2 of the supplementary material). This so-called "Urbach tail" is a well known feature in the band-edge spectra of solid-state materials,[40,41] but is also frequently observed for organic molecules in solution, often with a $1/k_BT$-dependent decay constant.[42–45] For molecules, this exponential tail and characteristic temperature dependence has been interpreted as the cumulative effect of hot-band transitions originating from the sparsely thermally-occupied excited levels of Franck-Condon active vibrations on the ground state. For all the coumarins, with the possible exception of C545, ω_{vis} falls within this Urbach region.

The fluorescence quantum yield ϕ and fractional spectral bandpass η_{bp} are listed in Table I. The optimal location of the instrument's emission bandpass depends on the interplay between the fluorophore's Stokes shift, fluorescence lineshape, and the pre-resonant shift on the order of $\omega_{IR} \approx$

ω_{10} required for FEIR resonance (i.e. Eq. (1)). A detection band on the Stokes side of ω_{vis} can in general only access a smaller portion of the emission spectrum than in a conventional one-photon resonant fluorescence excitation scheme due to this pre-resonant shift. For fluorophores with small Stokes shifts, placing the detection band on the anti-Stokes side of ω_{vis} could in principle allow for larger η_{bp}, with the added benefit of contending with the weaker anti-Stokes solvent Raman background. In this work we use a Stokes-side bandpass (Figure 2(c)) that relies on the relatively large Stokes shifts of the coumarin dyes (Table I), which for the most part greatly exceed ω_{10} for the vibrations under consideration. The decrease in η_{bp} from $\sim$0.4 to $\sim$0.1 when moving red to blue across the coumarin series is a consequence of the increasingly off-resonant FEIR excitation with Stokes-side detection. C153 is notable by its large $\sim$5000 cm^{-1} Stokes shift, which results in the second-highest η_{bp} in the series despite its position in the blue side of the series.

B. FTIR absorption spectra

FTIR spectra of the coumarin series are shown in Figure 3. The IR pulse spectrum used in each FEIR measurement is superimposed to indicate the vibrations being excited. The pulse is broadband with respect to the vibrational linewidths and spans multiple modes in each case. Below 1650 cm^{-1} in the spectral range shown are C=C ring vibrations localized predominantly on the coumarin core, while the lactone carbonyl stretching band appears above 1700 cm^{-1}. In many cases this carbonyl band shows considerable structure (e.g. the splitting especially prominent for C153 and C525), which is likely due to a Fermi resonance.[46,47] C334, C314, and C343 contain another carbonyl group in the electron-withdrawing substituent, which appears between 1650-1700 cm^{-1}. The center of the IR pulse spectrum ω_{IR} = 1620 cm^{-1} was chosen to maximize coverage of the highest frequency ring modes, which have similar character across the coumarin series, and, as shown below, are typically the most strongly FEIR active. In contrast to the large variation in electronic resonance created by the range of absorption frequencies, here the collection of vibrational modes being pumped are fairly similar in frequency and extinction. Nevertheless, the vibrational transition strength is a critical factor for FEIR brightness via Eq. (10), and any differences in IR-vibrational cross-section should be reflected in the strength of the signal. To characterize these differences given the spectrally broad excitation, we compute the overlap

$$\varepsilon_{IR} = \int \varepsilon_{vib}(\omega) S_{IR}(\omega) d\omega, \tag{14}$$

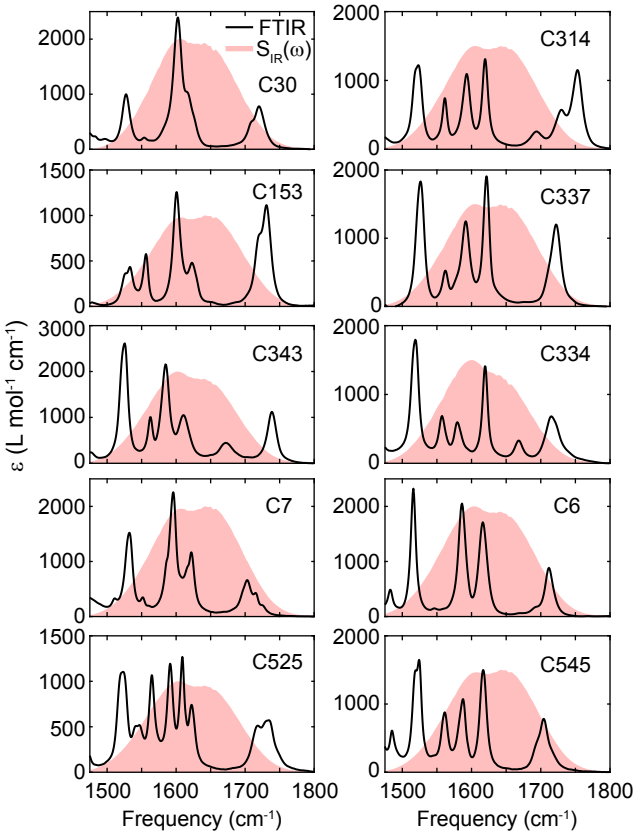

FIG. 3. FTIR spectra of the coumarin series in acetonitrile-d3 with the IR pulse spectrum $S_{\mathrm{IR}}(\omega)$ used for each FEIR measurement overlayed.

where $\varepsilon_{\mathrm{vib}}(\omega)$ is the vibrational extinction spectrum and $S_{\mathrm{IR}}(\omega)$ is the normalized IR spectral intensity profile. As shown in Figure S10 of the supplementary material, $\varepsilon_{\mathrm{IR}}$ only varies by a factor of $\sim$2 across the series.

C. Brightness analysis of high concentration FEIR data

Bulk FEIR measurements on 3 representative coumarins are shown in Figure 4 (complete series shown in Figure S5 of the supplementary material). High concentrations (30-100 μM) were used to keep the non-molecular background B negligibly small compared to the coumarin fluorescence. Panels (a)-(c) show the total detected photon rate F_{tot} from 2-pulse measurements in brightness units, that is, divided by $rC\eta_{\mathrm{bp}}I_{\mathrm{vis}}$. Instead of additionally dividing the FEIR component F by I_{IR} to recover q as in Eq. 9, it will be convenient for our analysis to work with an effective FEIR

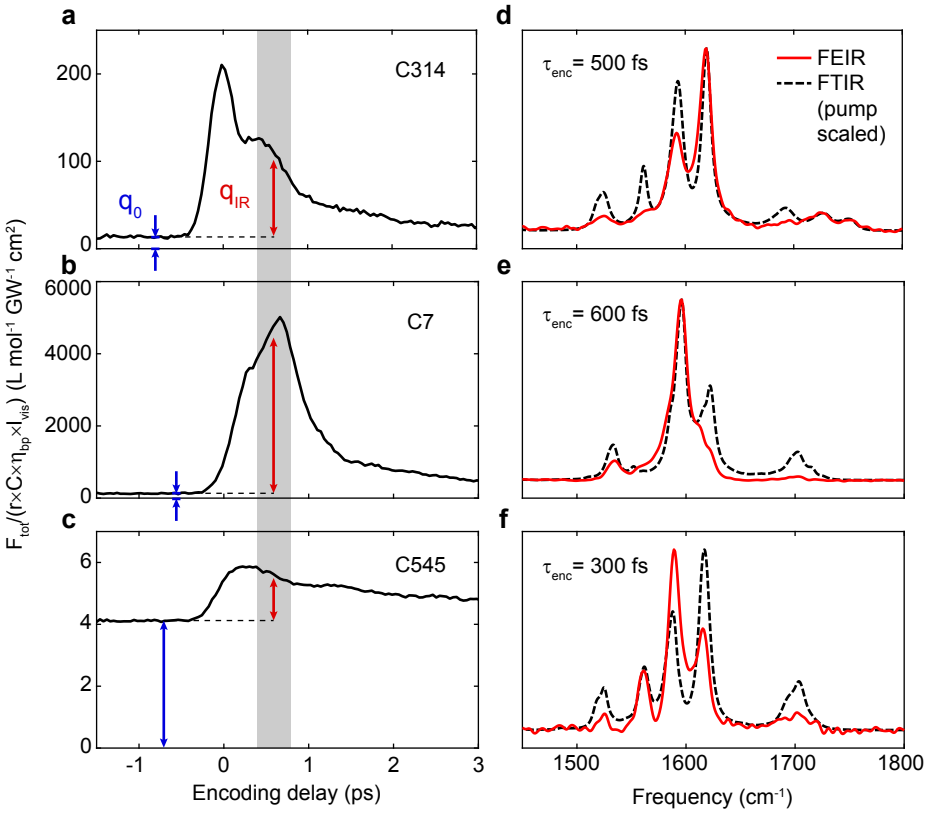

FIG. 4. (a)-(c) Total photon output F_{tot} from 2-pulse FEIR experiments plotted in brightness units for C314, C7, and C545, respectively. The effective FEIR and direct excitation brightness are indicated by arrows. (d)-(f) Comparison of IR pump spectrum-scaled FTIR spectra (dashed line) with FEIR spectrum (solid line) at the encoding delay indicated for each corresponding coumarin in (a)-(c). Each spectrum is independently normalized to its largest feature.

brightness where the IR intensity dependence has not been removed

$$q_{\text{IR}} = \frac{F}{rC\eta_{\text{bp}}I_{\text{vis}}} = qI_{\text{IR}}, \tag{15}$$

which has the same units as q_0, facilitating direct comparison of their respective magnitudes. Furthermore, because I_{IR} is held constant in this study, q_{IR} can still be compared between measurements on different molecules, and we will also refer to this quantity as the FEIR brightness unless further distinction is required. As B is negligible, q_0 is given by the constant offset (blue arrows) for $\tau_{\text{enc}} < 0$ where $F = 0$ by causality.

F reaches a maximum at early τ_{enc} before decaying away on a picosecond timescale due to vibrational relaxation processes (see Section 3 of the supplementary material for a note on the assignment of $\tau_{\text{enc}} = 0$). However, the details of the τ_{enc}-dependence near the maximum, notably

the peak position, vary for the different coumarins. As $F(\tau_{\text{enc}})$ measures the integrated response of the multiple vibrations within the IR bandwidth, some aspects of these differences reflect the variation in frequency spread, vibronic activity, and relaxation kinetics of the modes being sampled. To show which vibrations are contributing to the response in each case, Figures 4(d)-(f) show the corresponding FEIR spectra at selected early encoding delays superimposed on the IR pump-scaled FTIR spectra. In all cases, the high frequency ring modes between 1570-1620 cm^{-1} have the largest contribution to the F amplitude. Multimode coherence produces the strongly-damped oscillatory behavior present in some 2-pulse transients, which to some extent also plays a role in the location of the signal maximum. However, in the vicinity of $\tau_{\text{enc}} = 0$ the signal may also contain pulse-overlap artifacts, for example contributions from improperly ordered interactions of the IR and visible fields or vibrationally-nonresonant IR + visible two-photon absorption. We note that even in these cases the signal amplitude is still determined by the molecular response——one of the benefits of fluorescence detection which precludes non-resonant pulse-overlap contributions from the solvent or windows. Nevertheless, to avoid these potential complications, we will use the average value of $F(\tau_{\text{enc}})$ between 400 and 800 fs (gray region in Figures 4(a)-(c) with red arrow indicating the average) to define q_{IR} for our analysis. While this window safely avoids the pulse-overlap region, in many cases the excited vibrational population has already undergone partial relaxation which may result in artificially lower measured FEIR brightness (supplementary material Section 5 compares these FEIR brightnesses with those using the maximum F values).

The coumarins in Figure 4 were chosen to represent the full range of FEIR resonance conditions across the series; C314 being one of the bluest, C7 intermediate, and C545 the reddest. As evident from the y-axis scales of Figure 4(a)-(c), the brightness of the overall fluorescence $(F + F_0)$ increases dramatically for the redder coumarins. However, for C545 the direct excitation background has become larger than the FEIR signal. This reduction in contrast is evident in a much smaller modulation ratio of $M = 0.35$ for C545, compared to $M = 35$ for C7 and $M = 6.8$ for C314.

In Figure 5 we investigate how brightness and contrast are explicitly influenced by the FEIR resonance condition discussed in Section IV A. To normalize out variations in emission probability, we divide the FEIR and direct excitation brigthnesses by quantum yield ϕ. The resulting quantities q_{IR}/ϕ and q_0/ϕ are proportional to aI_{IR} and a_0, respectively, with the same proportionality constant. The quantity aI_{IR} may be interpreted as the effective cross-section seen by the visible pulse after vibrational excitation of the molecule with the IR pulse in our instrument. Figure

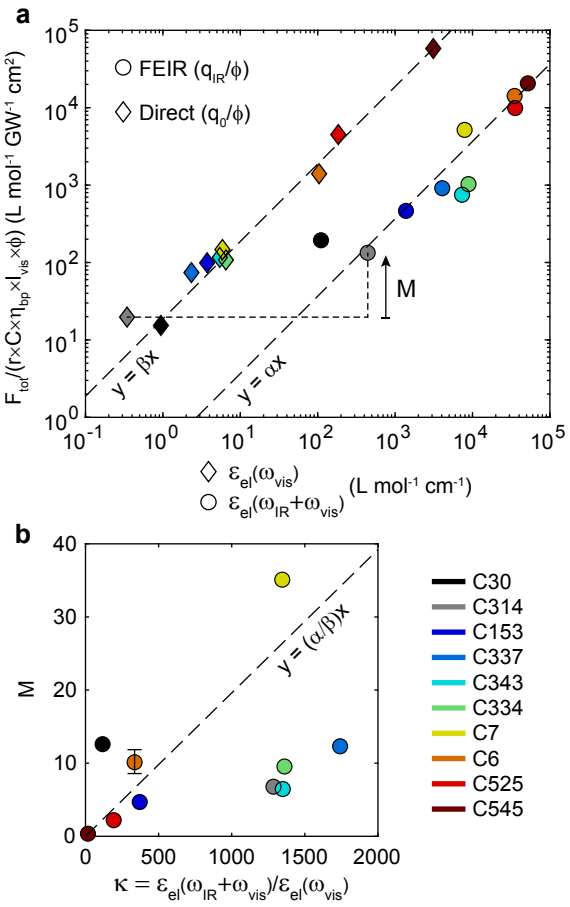

FIG. 5. (a) Correlation of q_{IR}/ϕ against $\varepsilon(\omega_{\mathrm{IR}}+\omega_{\mathrm{vis}})$ (circles), and q_0/ϕ against $\varepsilon(\omega_{\mathrm{vis}})$ (diamonds) on log-log axes. Linear fits in dashed lines have a slope of $\alpha = 0.367$ GW^{-1} cm^3 with $R^2 = 0.943$, and $\beta = 18.7$ GW^{-1} cm^3 with $R^2 = 0.999$. (b) Correlation of M against κ. The dashed line has slope given by α/β, the ratio of trend lines in panel (a). This ratio is slightly larger than the regression slope of M vs. κ (not shown).

5(a) shows that these proxies for the FEIR and direct excitation cross-sections are linearly related to the electronic extinction coefficient evaluated at $\omega_{\mathrm{IR}}+\omega_{\mathrm{vis}}$ and ω_{vis}, respectively, over several orders of magnitude. Logarithmic scaling is used to conveniently represent the multiple decades in each axis (same data on linear axes is shown in Figure S8 of the supplementary material).

The strong linear relationship between $\varepsilon_{\mathrm{el}}(\omega_{\mathrm{vis}})$ and q_0/ϕ indicates that linear absorption of the visible pulse is the primary contributor to the direct excitation background F_0 across the range of resonance conditions studied here, and we will consequently also refer to F_0 as the one-photon background. However, we note that for the bluest coumarins C30 and C314, the I_{vis}-dependence of F_0 becomes super-linear beyond the intensities used in Figure 5 (Figure S16 in the supplemen-

tary material), implying a cross-over to two-photon absorption being the dominant source of F_0 background for these deeply pre-resonant excitation conditions where $\varepsilon_{\mathrm{el}}(\omega_{\mathrm{vis}})$ is exceptionally small.

On the other hand, the linear relationship between $\varepsilon_{\mathrm{el}}(\omega_{\mathrm{IR}}+\omega_{\mathrm{vis}})$ and q_{IR}/ϕ (and by proportionality a), though more diffuse, is a more striking and *a priori* less obvious result. Taken exactly, a perfect linear relationship would indicate that the effective lineshape function of the encoding transition is simply given by the equilibrium absorption lineshape red-shifted by the vibrational frequency, i.e.

$$\Delta(\omega) \sim g_{\mathrm{el}}(\omega-\omega_{10}), \tag{16}$$

where $g_{\mathrm{el}}(\omega)$ is the normalized electronic lineshape function. While intuitive and in line with the heuristic double-resonance picture evoked by Eq. (1), this association cannot be formally exact, as in general both the initial and final states involved in the encoding transition are different from the bare electronic transition. The equilibrium lineshape $g_{\mathrm{el}}(\omega)$ is composed of multiple vibronic transitions involving the Franck-Condon active intramolecular coumarin vibrations—including, but importantly not limited to, the vibrations being interrogated by FEIR—as well as being broadened by overdamped solvation coordinates. While the vibronic contribution to $\Delta(\omega)$ from the mode being pumped is certainly different because the initial state is $v=1$ rather than $v=0$, it is reasonable to expect a similar contribution from the solvent, as, from the solvent's perspective, vibrational excitation on the ground-state is a small perturbation compared with electronic excitation. As the FEIR resonance conditions explored here probe the red-side of the transition where the breadth of the lineshape is likely dominated by the solvent contribution, Eq. (16) could therefore be a reasonable approximation. For coumarins on the blue side of the series, $\varepsilon_{\mathrm{el}}(\omega_{\mathrm{IR}}+\omega_{\mathrm{vis}})$ falls within the Urbach region of the lineshape, and it is possible that initial thermal population of low-frequency modes is important. A similar correspondence between signal size and resonance condition for $\omega_{\mathrm{vis}} < \omega_{0-0}-\omega_{\mathrm{IR}}$ was found in some of the original experiments of Kaiser and co-workers, although the vibrations being pumped were likely combination bands.[42] From a computational perspective, $\Delta(\omega)$ is related to the lineshape of the vibrationally pre-excited absorption spectrum introduced by Burghardt and coworkers to model the closely-related excitation process in vibrationally promoted electronic resonance (VIPER) spectroscopy.[48,49] Although their approach only investigated the effect of the intramolecular modes and did not treat broadening from the solvation environment explicitly, their results typically show a peak red-shifted from the 0-0 transition by roughly ω_{10} due primarily to the pre-excited mode's 1-0 vibronic transition.

These computational results support the frequency shift in Eq. (16) as well as the simplified energy level diagram in Figure 1.

The scatter in the $\varepsilon_{\mathrm{el}}(\omega_{\mathrm{IR}}+\omega_{\mathrm{vis}})$ vs. q_{IR}/ϕ trend is likely influenced by variations in the other terms in Eq. (10), i.e. the vibrational transition dipoles, Franck-Condon overlaps, and orientational factors. In fact, given that these factors are not accounted for, it is perhaps somewhat remarkable that a linear regression of this quality is even observed. This may be explained in the following ways. First, as the a values here reflect the collective response of multiple vibrations, the differences in these unaccounted factors are potentially smoothed out between dyes, thereby isolating the electronic resonance dependence for an "average" coumarin. Second, the structural similarity between the dyes likely precludes very large variations in these factors for the dominant core ring modes, while in contrast $\varepsilon_{\mathrm{el}}(\omega_{\mathrm{IR}}+\omega_{\mathrm{vis}})$ varies by almost 3 orders of magnitude. As mentioned in Section IV B, one way to account for the vibrational transition strength is by the factor ε_{IR} (Eq. (14)). However, using $\varepsilon_{IR}\cdot\varepsilon_{\mathrm{el}}(\omega_{\mathrm{IR}}+\omega_{\mathrm{vis}})$ as the x-values does not substantially improve the linear relationship (Figure S10 in the supplementary material), perhaps because the remaining factors play the dominant role. Uncontrolled differences in the instrument's alignment and errors in experimental parameters between measurements also contribute to uncertainty in the measured brightness values. We characterized day-to-day differences in q_{IR} and q_0 for C6, and found a coefficient of variation (standard deviation over mean) of 12% and 10%, respectively (Section 4 in the supplementary material). We expect this experimental uncertainty to be representative across the coumarin series, and it is smaller than the size of the data markers in Figure 5(a). Therefore, we believe that this scatter is predominantly reflective of differences in the vibrational mode-specific factors, of which the vibronic coupling is likely the most important.

Figure 5(b) shows the corresponding modulation ratios M (Eq. (3)) from the FEIR measurements in Figure 5(a). As B is negligible, M can be written as

$$M=(a/a_0)I_{\mathrm{IR}}, \tag{17}$$

which is manifested graphically as the signed distance (in log units) between respective y-values in Figure 5(a), (indicated for C314). The vertical error bar for C6 shows two standard deviations for the experimental uncertainty stated above. The M values are plotted against the extinction coefficient ratios

$$\kappa=\varepsilon_{\mathrm{el}}(\omega_{\mathrm{IR}}+\omega_{\mathrm{vis}})/\varepsilon_{\mathrm{el}}(\omega_{\mathrm{vis}}), \tag{18}$$

thereby effectively combining both trends in Figure 5(a). The relationship between these quantities

describes the extent to which the equilibrium absorption lineshape alone can predict the contrast in an FEIR experiment for given IR intensity. The resulting correlation is quite diffuse (Pearson correlation coefficient $r = 0.49$) primarily because the scatter in the q_{IR}/ϕ vs. $\varepsilon_{\mathrm{el}}(\omega_{\mathrm{IR}} + \omega_{\mathrm{vis}})$ trend caused by the unaddressed vibrational and vibronic factors is magnified. Additionally, noise on the small $\varepsilon_{\mathrm{el}}(\omega_{\mathrm{vis}})$ values for the bluer coumarins likely amplifies the uncertainty in their κ values, although we do not estimate the corresponding error bars. While M is correlated to κ, the relationship is not sufficiently good to be widely predictive in a quantitative sense, most likely due to the importance of the vibrational mode-specific factors.

However, some general observations about how the contrast depends on the relationship between $\varepsilon_{\mathrm{el}}(\omega)$, ω_{vis}, and ω_{10} can still be made. The order of magnitude smaller M value for C545 compared to the rest of the series is clearly due to the large one-photon background produced by ω_{vis} falling substantially higher on the absorption band tail (ω_{vis} at $\sim$6% of the band maximum). Even though C545 has the highest FEIR brightness in the series—which assuming Eq. (16) holds corresponds to fully maximized FEIR resonance—in practice measurements on this molecule suffer from lower signal to noise caused by the large shot noise introduced by F_0, requiring longer averaging times (Figure S5 in the supplementary material). Evidently, for the frequencies of vibration under consideration the electronic absorption edge is not sufficiently steep (quantified e.g. by $\Delta\omega_{\mathrm{edge}}$ in Table I, and Figures S1-S2 in the supplementary material) to allow maximal FEIR resonance without excessive one-photon background. How much direct band overlap, i.e. $\varepsilon_{\mathrm{el}}(\omega_{\mathrm{vis}})/\varepsilon_{\mathrm{el}}(\omega_{\mathrm{max}})$, can be tolerated in practice depends on how much slower a grows with $\varepsilon_{\mathrm{el}}(\omega_{\mathrm{IR}} + \omega_{\mathrm{vis}})$ than a_0 grows with $\varepsilon_{\mathrm{el}}(\omega_{\mathrm{vis}})$. This comparison may be quantified by the trend line slope ratio α/β = 2.0% (dashed line in Figure 5(b)). Because the detuning dependence is accounted for, this value describes on average the relative efficiency of FEIR excitation vs. direct one-photon excitation for a prototypical coumarin dye with the IR pulses of our instrument. Specifically, this value suggests that FEIR vibrational detection at maximal resonance is overall $\sim$50 times less efficient in these experiments than conventional fluorescence detection at maximal resonance. In terms of contrast, this implies that κ should be at least greater than $\sim$50 to achieve $M > 1$.

Even if the absorption edge is too broad to support maximal FEIR resonance with low one-photon background, detuning slightly could produce a workable compromise. For example, C6 has a similarly steep absorption edge as C545, but is detuned from maximal FEIR resonance by $\sim$900 cm^{-1}, putting $\omega_{\mathrm{IR}} + \omega_{\mathrm{vis}}$ and ω_{vis} at 63% and 0.19% of the band maximum, respectively

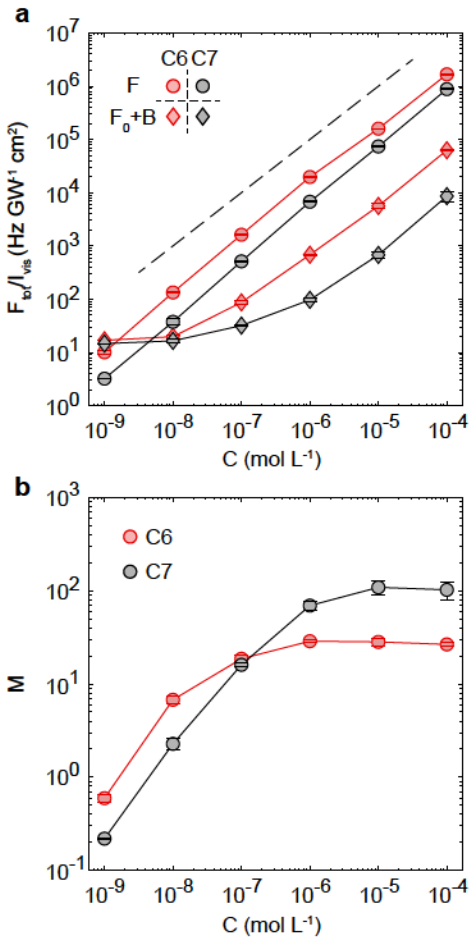

FIG. 6. (a) Concentration dependence of F/I_{vis} (circles) and $(F_0+B)/I_{\mathrm{vis}}$ (diamonds) for C6 (red) and C7 (black). The dashed line indicates a linear relationship between the log-scaled x- and y-axes to guide the eye. (b) M values corresponding to panel (a).

($\kappa = 340$). The resulting FEIR cross-section is ~0.7 times the size of that for C545, but with a ~40-fold decrease in one-photon background, leading to an excellent signal to background of $M \sim 10$.

D. Signal to background in the SM regime

The analysis in the previous section made use of high concentration measurements where essentially all of the detected light is dye fluorescence. As a per-molecule quantity, the construct of FEIR brightness is transferable to SM investigation, as is the brightness of the direct excitation background. However, in the low concentration regime where SM experiments operate, sources

of background independent of the target molecule, i.e. B, will usually play the dominant role in influencing contrast and signal to noise. To investigate the impact of B and how the practical considerations for contrast and signal to noise differ in the SM limit, we perform concentration-dependent measurements for two members of the coumarin series: C6 and C7. These molecules have similar FEIR spectra that are dominated by a single ring mode just below 1600 cm^{-1}, and likewise show similarly-shaped 2-pulse transients (Figure S4 in the supplementary material). C6 was previously used to demonstrated SM sensitivity in Ref. 21, and produces the second-brightest FEIR signal in the series. With the fixed resonance conditions of our instrument, C7 is $\sim 1/3$ as FEIR bright as C6, but displays an $\sim$3-fold higher B-free modulation ratio. As such, at high concentrations where I_{vis} can be varied to set the total fluorescence output at will, C7 is technically the better FEIR chromophore in terms of detection quality, although M is sufficiently high for both to be excellent. As mentioned in Section II B, the CaF_2 coverslips employed for the measurements in this section allowed for a $\sim$3-fold increase in FEIR brightness relative to the experiments in the previous section and Ref. 21, while maintaining a similar background size (cf. high-concentration M values in Figure 6 and Figure 5).

Figure 6(a) shows the concentration-dependence of the FEIR signal size F/I_{vis} and background $(F_0+B)/I_{\mathrm{vis}}$ from 100 μM to 1 nM for both molecules (complete FEIR data is provided in Section 6 of the supplementary material). In this representation, the effect of increasing I_{vis} to achieve reasonable count rates as C is lowered is normalized out to isolate the C-dependence across 5 orders of magnitude. For both dyes the FEIR component decreases roughly linearly with C. The lowest concentration points fall slightly below a linear dependence, which may be due to a saturation effect as discussed below, or could be caused by systematic error in the concentration from the serial dilution procedure. On the other hand, the background is linear in C at high concentrations, but in the low-C limit approaches a C-independent value which is the same for both coumarins: $\sim$15 Hz GW^{-1} cm^2, which can be assigned as the b coefficient in Eq. 13. This reflects the change from the background being dominated by F_0 at high C to being almost entirely composed of B in the nM range. As shown in Ref. 21, the distribution of photon arrival times for measurements in the nM range is dominated by a prompt component absent at high C, which suggests that solvent Raman scattering is likely the major contributor to B. As shown in that work, time-gating photon detection to exclude this prompt component can therefore increase M and the SNR, however we will not discuss this approach further here.

The C-dependence of the corresponding modulation ratios is shown in Figure 6(b). At high

concentrations M is C-independent because $F_0 \gg B$ (i.e. Eq. (17) holds) and the empirical contrast guidelines discussed in Section IV C apply. However, below a certain concentration M begins to fall as the dye's fluorescence must compete with the C-independent B background, and at SM equivalent concentrations ($\sim$1 nM, see below) M is 1-3 orders of magnitude lower than its high-C limit. The threshold concentration below which M decreases is notably lower for C6 than C7, and results in a crossing of their M vs. C curves at $\sim$100 nM. As a result C6 is distinctly the better SM FEIR chromophore under these resonance conditions, although C7 can still be detected at SM equivalent concentrations due to the $\sim$3-fold increase in FEIR signal facilitated by the updated sample configuration. This difference in bulk versus SM signal to background reflects a crossover from prioritizing a large F vs. F_0 contrast to prioritizing the brightness of overall fluorescence $F + F_0$ against B. As long as the high-C limit of the modulation ratio is sufficiently large, say $M > 1$, we can define a limiting concentration C_{lim} where the F and B rates are predicted to be equal based on FEIR brightness, and below which FEIR detection becomes increasingly impractical,

$$C_{\text{lim}} = \frac{b/r}{q_{\text{IR}}\eta_{\text{bp}}}. \tag{19}$$

The potential for SM detectability of an FEIR chromophore can then be simply assessed from a high concentration measurement by how close the calculated C_{lim} is to the SM-equivalent concentration (Figure S13 in the supplementary material). For example, we predict that C525 and C545 would also be possible SM FEIR candidates under the current resonance conditions, as at high-C we expect an increase to $M \sim 1$ for C545 with the new sample configuration.

In the range where F, F_0, and B each grow linearly with visible intensity, the signal to noise of a measurement may be improved by increasing I_{vis} while M remains constant, e.g. Eq. (4) predicts improvement by $\sim \sqrt{I_{\text{vis}}}$. In practice, however, saturation effects in the encoding transition set a limit on how large I_{vis} can usefully be made while still increasing the SNR. Figure 7 shows the I_{vis}-dependence of the FEIR signal size, here represented as F/C, for C6 and C7. Data from the entire concentration range in Figure 6 has been used in order to access both very low and high I_{vis} while keeping F_{tot} within the linear range of photon counting, and dividing F by C collapses the points onto a common saturation curve for each coumarin (log-scale plot in Figure S14). Figure 6 uses the lowest I_{vis} point for each concentration, which at the lowest concentrations nevertheless lies near the onset of saturation, which may partially explain the deviation from a linear F/I_{vis} vs. C relationship in Figure 6(a) mentioned above.

In general, the intensity-dependent form of saturation is influenced by the temporal characteris-

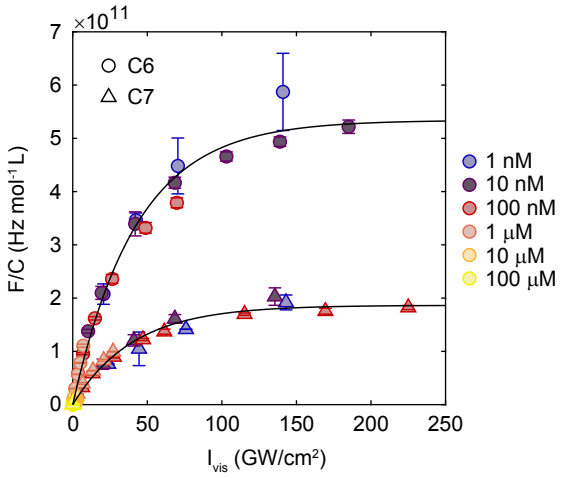

FIG. 7. Saturation of the encoding transition. F/C as a function of I_{vis} for C6 (circles) and C7 (triangles). C is indicated by color, and black lines are fits to the exponential model described in the text.

TABLE II. Saturation curve fit parameters for the exponential model $c(1-\exp(-I_{\text{vis}}/I_S))$ including 95% confidence intervals from the fitting routine.

Dye	c (Hz mol^{-1} L)	I_S (GW cm^{-2})
C6	$5.3\times10^{11}\pm0.3\times10^{11}$	42 ± 6
C7	$1.9\times10^{11}\pm0.1\times10^{11}$	40 ± 5

tics of excitation. For a two-level system with cw pumping, the steady-state upper level population, and hence the emission rate, saturates with the hyperbolic form

$$p_{ss} = \frac{\sigma I_{\text{vis}}/\hbar\omega_{\text{vis}}}{1+I_{\text{vis}}/I_S}, \tag{20}$$

where the saturation intensity is $I_S = \hbar\omega_{\text{vis}}/(2\sigma\tau_{\text{fl}})$, τ_{fl} is the fluorescence lifetime, and σ the absorption cross-section.[50] However, for pulsed excitation where the pulse duration t_{vis} is much shorter than τ_{fl} while the repetition period τ_{rep} is simultaneously much longer than τ_{fl}, the excited population immediately after each pulse is

$$p_{max} = \frac{1}{2}\Big(1-\exp(-I_{\text{vis}}/I_S)\Big), \tag{21}$$

where $I_S = \hbar\omega_{\text{vis}}/(2\sigma t_{\text{vis}})$.[51,52] The lower level population fully recovers before the next pulse arrives, and the average fluorescence output is therefore proportional to p_{max}. Our experiments operate in this short pulse limit ($t_{\text{vis}} \approx 300$ fs, $\tau_{\text{fl}} \approx 1$ ns, $\tau_{\text{rep}} \approx 1$ μs) and fits to the measured

saturation curves using this exponential model are shown in Figure 7 with fit parameters listed in Table II. In line with their relative FEIR brightnesses, F saturates at $\sim$3 times higher count rates for C6 than C7. However, the threshold intensities I_S extracted from the fits are the same within error, which is surprising given that I_S should be inversely proportional to the cross-section of the transition, and aI_{IR} is $\sim$3 times smaller for C7 compared to C6. Other photophysical mechanisms that sequester population, like intersystem crossing to triplet states, could also be playing a role in the saturation threshold.[53] Perhaps more importantly, treating the initial and final states of the encoding transition as a simple two-level system is likely not a reasonable assumption to describe the observed saturation behavior. So far we have not observed a similar saturation behavior in I_{IR}, although a more careful investigation is needed.

The background continues to grow roughly linearly in I_{vis} over the same range of intensities (Figure S14 in the supplementary material). Therefore, the contrast degrades as I_{vis} is increased into the saturating regime, leading to an eventual decrease in SNR. We find that a practical compromise is to operate near the saturation threshold I_S. Regardless of the mechanism, saturation leads to an increase in the effective size of the visible probe volume because the spatial distribution of excitation efficiency flattens out near the center of the focus but continues to increase in the wings.[54] At a given concentration the average number of molecules $\langle N \rangle$ in the probe volume therefore increases with I_{vis}, and determination of $\langle N \rangle$ by FEIR-CS is intensity-dependent. We measure $\langle N \rangle = 0.7$ for 1 nM C6 via FEIR-CS at the saturation threshold $I_{\mathrm{vis}} = 42$ GW cm^{-2}, which from the 2-pulse transient at the same intensity yields an F count rate per molecule of 480 Hz (see Figures S17 and S11 in the supplementary material, respectively). While FEIR-CS was not performed on the 1 nM C7 solution, assuming equivalent $\langle N \rangle$ at the same I_{vis} gives a lower count rate per molecule of 150 Hz, and the signal to noise of the 2-pulse signal is also correspondingly lower (cf. Figures S10 and S11 in the supplementary material). To facilitate comparison with existing SM optical methods it is useful to estimate the overall excitation probability P_{ex}. Considering our estimate for the total detection efficiency of fluorescence from C6 ($\eta \approx 1.3\%$), its quantum yield ($\phi = 0.89$), and the repetition-rate (994.7 kHz), this measured count rate per molecule corresponds to $P_{ex} \approx 4.2\%$. If this is indeed at the saturation threshold for the encoding transition (i.e. at $(1 - 1/e)$ of the saturated transition probability of 50%), this P_{ex} value implies a 13% IR-vibrational excitation probability. In this case we would expect that meaningful improvements to the overall excitation efficiency can still be made with larger IR fields.

V. CONCLUSIONS

In this work, we have examined some of the practical spectroscopic aspects of optimizing an FEIR experiment for bulk and SM vibrational detection. For a given molecule and vibration, the FEIR resonance condition is the most important aspect of experimental optimization. As ω_{IR} must always be tuned to cover the vibrational transition, this resonance condition amounts to a selection of ω_{vis} that efficiently brings the vibrationally-excited molecule to the electronic excited state. Our experimental results indicate that the electronic absorption spectrum is a useful guide for this selection, specifically that the brightness of the FEIR signal scales linearly with $\varepsilon_{\mathrm{el}}(\omega_{\mathrm{IR}} + \omega_{\mathrm{vis}})$ on the low-frequency side of the band. However, optimizing the resonance condition is also constrained by the background fluorescence from direct visible excitation, which for all but the most deeply pre-resonant cases is caused by linear absorption and hence proportional to $\varepsilon_{\mathrm{el}}(\omega_{\mathrm{vis}})$. For bulk measurements, keeping this fluorescence background small compared to the FEIR signal is the primary consideration for high signal to noise data acquisition. To this end, depending on the shape of the electronic absorption edge and particularly the fall-off of its red wing, bulk FEIR detection can be improved by detuning the resonance condition. In the SM regime, however, background is dominated by sources independent of the target molecule and signal photons are scarce, so the resonance condition should be adjusted to increase the absolute brightness of the FEIR signal at the expense of more one-photon background. Saturation of the encoding transition in the visible intensity limits the maximum photon count rates that can be achieved, although further improvements to the IR-vibrational excitation efficiency are likely still available.

Although the experiments presented here utilized a series of dyes with variable electronic spectra against a fixed ω_{vis}, we have framed the discussion of resonance conditions from the perspective of a tunable ω_{vis}. Indeed, our results indicate that being able to freely adjust ω_{vis} to carefully optimize resonance for the chromophore at hand will significantly improve the versatility of FEIR spectroscopy, and represents an important technical step towards its application to more general SM vibrational investigation. Additionally, a wide tuning range will facilitate the selection of fluorophores across the entire visible spectrum as potential FEIR candidates. While the equilibrium electronic spectrum can be used to predict the effect of resonance, our results also show that it alone is not sufficient to predict FEIR brightness and that substantial variations occur even for similar-character vibrations of the structurally-related coumarin dyes we studied. Therefore, a more detailed understanding of vibrational mode-specific factors will be crucial for predicting

which vibrations on different families of fluorophores can be used as FEIR probes. In particular, we are interested in understanding the symmetry and structural properties required of a fluorophore to exhibit FEIR bright vibrations, and to what extent various spectroscopically useful probe vibrations, e.g. local carbonyl stretching modes, can be made sufficiently FEIR active to yield SM sensitivity.

The largest SM signal count rates (480 Hz) achieved with our current implementation of FEIR spectroscopy are still low compared with the few to hundreds of kHz rates commonly encountered in modern solution-phase SM fluorescence experiments.[55–58] From the perspective of photon budget, further improvement beyond this level would likely be required to successfully implement SM dynamics measurements based on the direct analysis of signal intensity trajectories. With our current signal levels, however, one route towards accessing kinetic information from real-time SM fluctuations is through correlation spectroscopy (CS) methods analogous to fluorescence correlation spectroscopy and related techniques.[59,60] These methods measure ensemble-averaged kinetic timescales via time-correlation functions of signal fluctuations that arise from the dynamics of individual molecules transiently occupying the probe volume. Because the time-resolution of a correlation function is not degraded by time-averaging, CS methods can use longer data acquisition times when signal levels are small, and are also less susceptible to photobleaching as diffusion replenishes the probe volume with new molecules. The FEIR-CS measurements used here and in Ref. 21 to characterize SM sensitivity demonstrate the basic feasibility of this approach. Potential FEIR-CS experiments could leverage changes in a molecule's vibrational spectrum to isolate the persistence of specific chemical structures or follow how reactants and products interconvert on microsecond timescales. For example, local-mode vibrational probes could be used to address the impact of site-specific interactions like hydrogen-bonding or ion association on molecular transport in complex environments. Similarly, FEIR-CS experiments could track the formation and breaking of specific intermolecular contacts between reactive partners during the initial diffusive encounter and subsequent binding in diffusion-limited bimolecular reactions.

Multiple routes exist for increasing SM FEIR signal sizes. Increasing the pulse repetition-rate beyond the current 1 MHz would have the greatest impact on accessing higher count rates. While the repetition-rate scalability of generating nJ-level sub-ps mid-IR pulses has technical challenges, increases by a factor of $\sim$10 with reduced pulse energy and bandwidth are feasible. When coupled with higher NA focusing of the IR, sufficiently large IR-vibrational excitation rates should still be accessible. Important gains in detection efficiency are also expected through increasing the

NA of fluorescence collection, which at 0.8 is currently low compared to typical SM fluorescence experiments. With these improvements, we believe more useful kHz-level SM FEIR count rates should be accessible.

SUPPLEMENTARY MATERIAL

See the supplementary material for details on the coumarin low-frequency electronic absorption edges, photon pile-up correction, complete coumarin series FEIR data and acquisition details, estimation of experimental uncertainty in brightness, comparison of alternative brightness values, concentration and visible intensity dependent FEIR data for C6 and C7, and determination of $\langle N \rangle$ for C6 by FEIR-CS.

ACKNOWLEDGEMENTS

This work was supported by a grant from the National Science Foundation (CHE-1856684). Steady-state electronic absorption and fluorescence characterization made use of the shared facilities at the University of Chicago Materials Research Science and Engineering Center, supported by the National Science Foundation under award number DMR-2011854.

DATA AVAILABILITY

The data that support the findings of this study are available from the corresponding author upon reasonable request.

REFERENCES

[1]S. Nie and S. R. Emory, "Probing single molecules and single nanoparticles by surface-enhanced Raman scattering," Science **275**, 1102–1106 (1997).

[2]K. Kneipp, Y. Wang, H. Kneipp, L. T. Perelman, I. Itzkan, R. R. Dasari, and M. S. Feld, "Single molecule detection using surface-enhanced Raman scattering (SERS)," Phys. Rev. Lett. **78**, 1667–1670 (1997).

[3]E. C. Le Ru and P. G. Etchegoin, "Single-molecule surface-enhanced Raman spectroscopy," Annu. Rev. Phys. Chem. **63**, 65–87 (2012).

[4]M. D. Sonntag, E. A. Pozzi, N. Jiang, M. C. Hersam, and R. P. Van Duyne, "Recent advances in tip-enhanced Raman spectroscopy," J. Phys. Chem. Lett. **5**, 3125–3130 (2014).

[5]Y. Yu, T.-H. Xiao, Y. Wu, W. Li, Q.-G. Zeng, L. Long, and Z.-Y. Li, "Roadmap for single-molecule surface-enhanced Raman spectroscopy," Adv. Photonics **2**, 1 – 20 (2020).

[6]X. G. Xu, M. Rang, I. M. Craig, and M. B. Raschke, "Pushing the sample-size limit of infrared vibrational nanospectroscopy: From monolayer toward single molecule sensitivity," J. Phys. Chem. Lett. **3**, 1836–1841 (2012).

[7]T. Tanaka, T. Yano, and R. Kato, "Nanostructure-enhanced infrared spectroscopy," Nanophotonics (2021).

[8]F. S. Ruggeri, B. Mannini, R. Schmid, M. Vendruscolo, and T. P. J. Knowles, "Single molecule secondary structure determination of proteins through infrared absorption nanospectroscopy," Nat. Commun. **11**, 1–9 (2020).

[9]W. Ho, "Single-molecule chemistry," J. Chem. Phys. **117**, 11033–11061 (2002).

[10]A. Laubereau, A. Seilmeier, and W. Kaiser, "A new technique to measure ultrashort vibrational relaxation times in liquid systems," Chem. Phys. Lett. **36**, 232–237 (1975).

[11]A. Seilmeier and W. Kaiser, "Ultrashort intramolecular and intermolecular vibrational energy transfer of polyatomic molecules in liquids," in *Ultrashort Laser Pulses: Generation and Applications*, edited by W. Kaiser (Springer Berlin Heidelberg, Berlin, Heidelberg, 1993) pp. 279–317.

[12]H.-J. Hübner, M. Wörner, W. Kaiser, and A. Seilmeier, "Subpicosecond vibrational relaxation of skeletal modes in polyatomic molecules," Chem. Phys. Lett. **182**, 315–320 (1991).

[13]T. Dahinten, J. Baier, and A. Seilmeier, "Vibrational energy transfer processes in dye molecules after ultrafast excitation of skeletal modes," Chem. Phys. **232**, 239–245 (1998).

[14]J. C. Wright, "Double resonance excitation of fluorescence in the condensed phase—an alternative to infrared, Raman, and fluorescence spectroscopy," Appl. Spectrosc. **34**, 151–157 (1980).

[15]M. J. Winterhalder, A. Zumbusch, M. Lippitz, and M. Orrit, "Toward far-field vibrational spectroscopy of single molecules at room temperature," J. Phys. Chem. B **115**, 5425–5430 (2011).

[16]H. Xiong, L. Shi, L. Wei, Y. Shen, R. Long, Z. Zhao, and W. Min, "Stimulated Raman excited fluorescence spectroscopy and imaging," Nat. Photonics **13**, 412–417 (2019).

[17]H. Xiong and W. Min, "Combining the best of two worlds: Stimulated Raman excited fluorescence," J. Chem. Phys. **153**, 210901 (2020).

[18]J. N. Mastron and A. Tokmakoff, "Two-photon-excited fluorescence-encoded infrared spectroscopy," J. Phys. Chem. A **120**, 9178–9187 (2016).

[19]J. N. Mastron and A. Tokmakoff, "Fourier transform fluorescence-encoded infrared spectroscopy," J. Phys. Chem. A **122**, 554–562 (2018).

[20]L. Whaley-Mayda, S. B. Penwell, and A. Tokmakoff, "Fluorescence-encoded infrared spectroscopy: Ultrafast vibrational spectroscopy on small ensembles of molecules in solution," J. Phys. Chem. Lett. **10**, 1967–1972 (2019).

[21]L. Whaley-Mayda, A. Guha, S. B. Penwell, and A. Tokmakoff, "Fluorescence-encoded infrared vibrational spectroscopy with single-molecule sensitivity," J. Am. Chem. Soc. **143**, 56 (2021).

[22]C. Würth, M. Grabolle, J. Pauli, M. Spieles, and U. Resch-Genger, "Relative and absolute determination of fluorescence quantum yields of transparent samples," Nat. Protoc. **8**, 1535–1550 (2013).

[23]S. B. Penwell, L. Whaley-Mayda, and A. Tokmakoff, "Single-stage MHz mid-IR OPA using $LiGaS_2$ and a fiber laser pump source," Opt. Lett. **43**, 1363 (2018).

[24]D. R. Sandison and W. W. Webb, "Background rejection and signal-to-noise optimization in confocal and alternative fluorescence microscopes," Appl. Opt. **33**, 603–615 (1994).

[25]D. R. Sandison, D. W. Piston, R. M. Williams, and W. W. Webb, "Quantitative comparison of background rejection, signal-to-noise ratio, and resolution in confocal and full-field laser scanning microscopes," Appl. Opt. **34**, 3576–3588 (1995).

[26]S. T. Hess and W. W. Webb, "Focal volume optics and experimental artifacts in confocal fluorescence correlation spectroscopy," Biophys. J. **83**, 2300–2317 (2002).

[27]L. D. Lavis and R. T. Raines, "Bright ideas for chemical biology," ACS Chem. Biol. **3**, 142–155 (2008).

[28]L. D. Lavis and R. T. Raines, "Bright building blocks for chemical biology," ACS Chem. Biol. **9**, 855–866 (2014).

[29]Y. Tian, J. Halle, M. Wojdyr, D. Sahoo, and I. G. Scheblykin, "Quantitative measurement of fluorescence brightness of single molecules," Methods Appl. Fluoresc. **2**, 035003 (2014).

[30]Eq. (6) neglects a negative contribution to F due to depletion of the equilibrium ground state by the IR pump which consequently reduces the amount of fluorescence from direct visible excitation. For the resonance conditions considered in this work, this depletion contribution is negligible compared to the proper FEIR excited contribution (i.e. described by P_{ex}), and we will not consider its effect in our analysis.

[31]A. Giudice, M. Ghioni, R. Biasi, F. Zappa, S. Cova, P. Maccagnani, and A. Gulinatti, "High-rate photon counting and picosecond timing with silicon-SPAD based compact detector modules," J. Mod. Opt. **54**, 225–237 (2007).

[32]Z. W. Fox, T. J. Blair, and M. Khalil, "Determining the orientation and vibronic couplings between electronic and vibrational coordinates with polarization-selective two-dimensional vibrational-electronic spectroscopy," J. Phys. Chem. Lett. , 1558–1563 (2020).

[33]J. D. Gaynor, R. B. Weakly, and M. Khalil, "Multimode two-dimensional vibronic spectroscopy. I. Orientational response and polarization-selectivity," J. Chem. Phys. **154**, 184201 (2021).

[34]J. M. Kauffman, "Laser dye structures and synonyms," Appl. Opt. **19**, 3431–3435 (1980).

[35]K. H. Drexhage, "Structure and properties of laser dyes," in *Dye Lasers*, edited by F. P. Schäfer (Springer Berlin Heidelberg, Berlin, Heidelberg, 1973) pp. 144–193.

[36]G. Reynolds and K. Drexhage, "New coumarin dyes with rigidized structure for flashlamp-pumped dye lasers," Opt. Commun. **13**, 222–225 (1975).

[37]X. Liu, J. M. Cole, P. G. Waddell, T.-C. Lin, J. Radia, and A. Zeidler, "Molecular origins of optoelectronic properties in coumarin dyes: Toward designer solar cell and laser applications," J. Phys. Chem. A **116**, 727–737 (2012).

[38]J. B. Birks, *Photophysics of Aromatic Molecules* (Wily-Interscience, London, 1973).

[39]A. S. Tarleton, J. C. Garcia-Alvarez, A. Wynn, C. M. Awbrey, T. P. Roberts, and S. Gozem, "OS100: A benchmark set of 100 digitized UV–visible spectra and derived experimental oscillator strengths," J. Phys. Chem. A **126**, 435–443 (2022).

[40]F. Urbach, "The long-wavelength edge of photographic sensitivity and of the electronic absorption of solids," Phys. Rev. **92**, 1324–1324 (1953).

[41]J. D. Dow and D. Redfield, "Toward a unified theory of Urbach's rule and exponential absorption edges," Phys. Rev. B **5**, 594–610 (1972).

[42]F. Wondrazek, A. Seilmeier, and W. Kaiser, "Ultrafast intramolecular redistribution and intermolecular relaxation of vibrational energy in large molecules," Chem. Phys. Lett. **104**, 121–128 (1984).

[43]P. O. J. Scherer, A. Seilmeier, and W. Kaiser, "Ultrafast intra- and intermolecular energy transfer in solutions after selective infrared excitation," J. Chem. Phys. **83**, 3948–3957 (1985).

[44]S. Kinoshita, N. Nishi, A. Saitoh, and T. Kushida, "Urbach tail of organic dyes in solution," J. Phys. Soc. Japan **56**, 4162–4175 (1987).

[45]D. Bingemann, A. M. King, and F. F. Crim, "Transient electronic absorption of vibrationally excited CH_2I_2: Watching energy flow in solution," J. Chem. Phys. **113**, 5018–5025 (2000).

[46]R. N. Jones, C. L. Angell, T. Ito, and R. J. D. Smith, "The carbonyl stretching bands in the infrared spectra of unsaturated lactones," Can. J. Chem. **37**, 2007–2022 (1959).

[47]C. Chudoba, E. T. J. Nibbering, and T. Elsaesser, "Site-specific excited-state solute-solvent interactions probed by femtosecond vibrational spectroscopy," Phys. Rev. Lett. **81**, 3010–3013 (1998).

[48]J. von Cosel, J. Cerezo, D. Kern-Michler, C. Neumann, L. J. G. W. van Wilderen, J. Bredenbeck, F. Santoro, and I. Burghardt, "Vibrationally resolved electronic spectra including vibrational pre-excitation: Theory and application to VIPER spectroscopy," J. Chem. Phys. **147**, 164116 (2017).

[49]L. J. G. W. van Wilderen, A. T. Messmer, and J. Bredenbeck, "Mixed IR/Vis two-dimensional spectroscopy: Chemical exchange beyond the vibrational lifetime and sub-ensemble selective photochemistry," Angew. Chem. Int. Ed. **53**, 2667–2672 (2014).

[50]W. E. Moerner and D. P. Fromm, "Methods of single-molecule fluorescence spectroscopy and microscopy," Rev. Sci. Instrum. **74**, 3597–3619 (2003).

[51]R. I. Ghauharali, M. Müller, A. H. Buist, T. S. Sosnowski, T. B. Norris, J. Squier, and G. J. Brakenhoff, "Optical saturation measurements of fluorophores in solution with pulsed femtosecond excitation and two-dimensional CCD camera detection," Appl. Opt. **36**, 4320–4328 (1997).

[52]R. Loudon, *The Quantum Theory of Light*, 3rd ed. (Oxford University Press, Oxford, 2000).

[53]J. Humpolíčková, A. Benda, and J. Enderlein, "Optical saturation as a versatile tool to enhance resolution in confocal microscopy," Biophys. J. **97**, 2623–2629 (2009).

[54]I. Gregor, D. Patra, and J. Enderlein, "Optical saturation in fluorescence correlation spectroscopy under continuous-wave and pulsed excitation," ChemPhysChem **6**, 164–170 (2005).

[55]T. Ha and P. Tinnefeld, "Photophysics of fluorescent probes for single-molecule biophysics and super-resolution imaging," Annu. Rev. Phys. Chem. **63**, 595–617 (2012).

[56]Q. Wang and W. E. Moerner, "Lifetime and spectrally resolved characterization of the photodynamics of single fluorophores in solution using the anti-brownian electrokinetic trap," J. Phys. Chem. B **117**, 4641–4648 (2013).

[57]J.-Y. Kim and H. S. Chung, "Disordered proteins follow diverse transition paths as they fold and bind to a partner," Science **368**, 1253–1257 (2020).

[58]S. Hou, J. Exell, and K. Welsher, "Real-time 3D single molecule tracking," Nat. Commun. **11**, 1–10 (2020).

[59]O. Krichevsky and G. Bonnet, "Fluorescence correlation spectroscopy: the technique and its applications," Rep. Prog. Phys. **65**, 251 (2002).

[60]E. L. Elson, "Fluorescence correlation spectroscopy: Past, present, future," Biophys. J. **101**, 2855–2870 (2011).

Supplementary Material for:

Resonance conditions, detection quality, and single-molecule sensitivity in fluorescence-encoded infrared vibrational spectroscopy

Lukas Whaley-Mayda[†], Abhirup Guha[†], and Andrei Tokmakoff[†*]

[†]Department of Chemistry, James Franck Institute, and Institute for Biophysical Dynamics, The University of Chicago, Illinois 60637, United States
[*]Corresponding Author: Email: tokmakoff@uchicago.edu

Contents

S1 Low-frequency electronic absorption tails

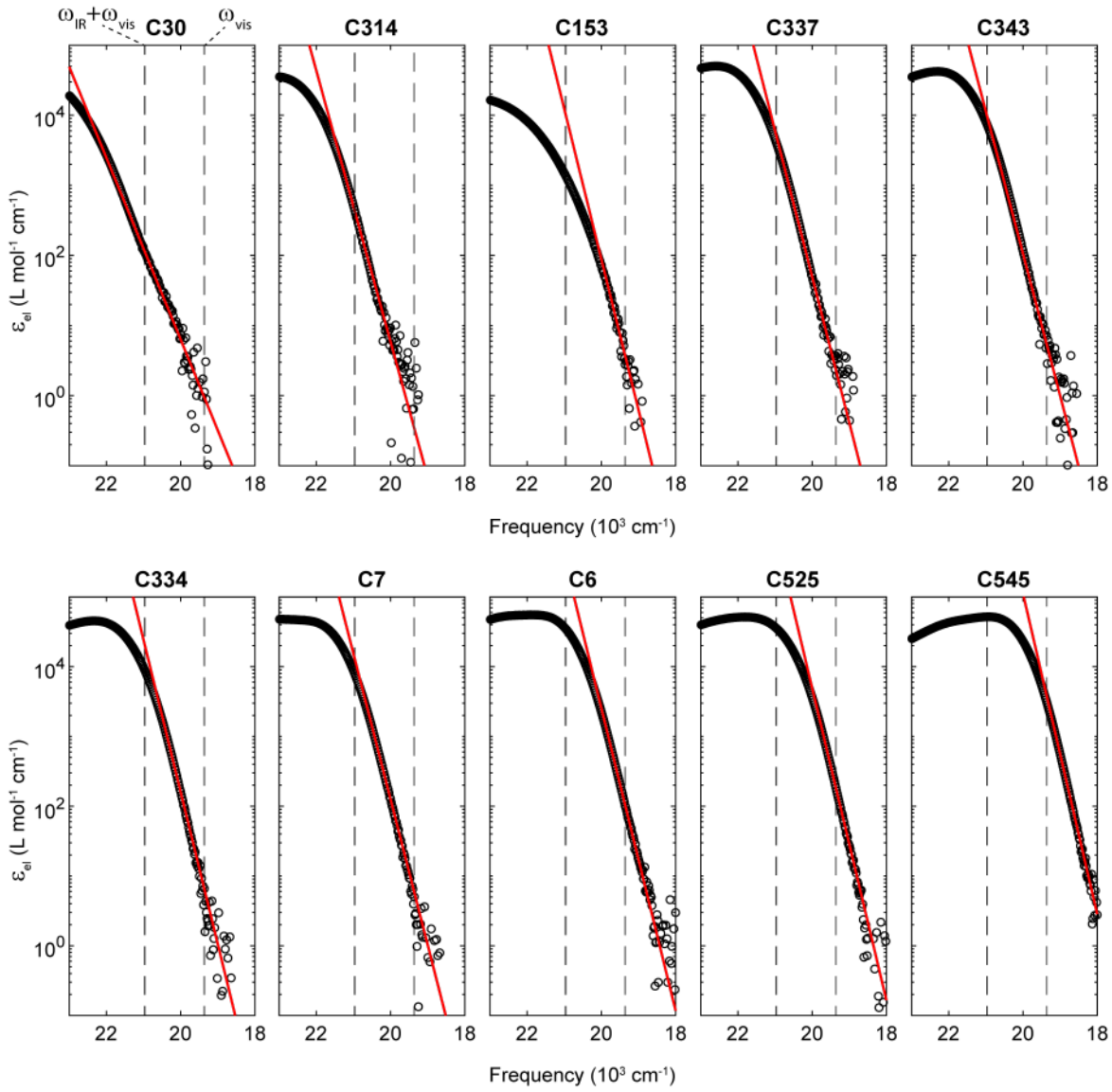

Figure S1: Low-frequency electronic extinction spectra (black circles) for each coumarin on a log y-scale, with fits of the Urbach region to an exponential (red). ω_{vis} and $\omega_{\mathrm{IR}} + \omega_{\mathrm{vis}}$ are indicated by dotted lines.

As shown in Figure S1, for all but the reddest 3 coumarins in the series (C6, C525, C545) the extinction spectrum at ω_{vis} is just above or within the noise floor of the absorption measurement. To extract the value of $\varepsilon(\omega_{\mathrm{vis}})$, we fit the band tail to an exponential $a\exp(k_{\mathrm{edge}}\omega)$, which describes the band shape in the low-frequency Urbach region, as described in the main text. In the case of C30 and C314, this fit essentially provides an extrapolation as $\varepsilon(\omega_{\mathrm{vis}})$ is solidly in the noise floor. The fitted decay constants k_{edge} are plotted in Figure S2.

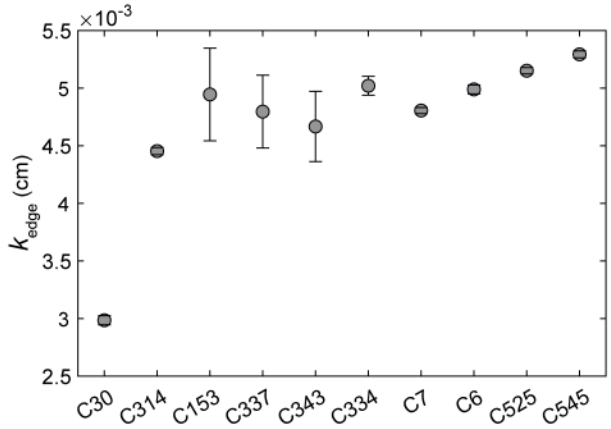

Figure S2: Exponential decay parameter k_{edge} from the fits to the low-frequency absorption edge in Figure S1. Error bars represent 95% confidence intervals from the fit routine.

S2 Correction to count rates for photon pile-up error

For large fluorescence intensities, single-photon counting is practically limited by the speed at which the detector can reset itself between photon arrivals, which can lead to artifacts as photons are missed. Errors of this nature are often referred to as photon pile-up.[1] Here we analyze the specific kind of pile-up error which manifests as a sub-linear response in our experimental configuration.

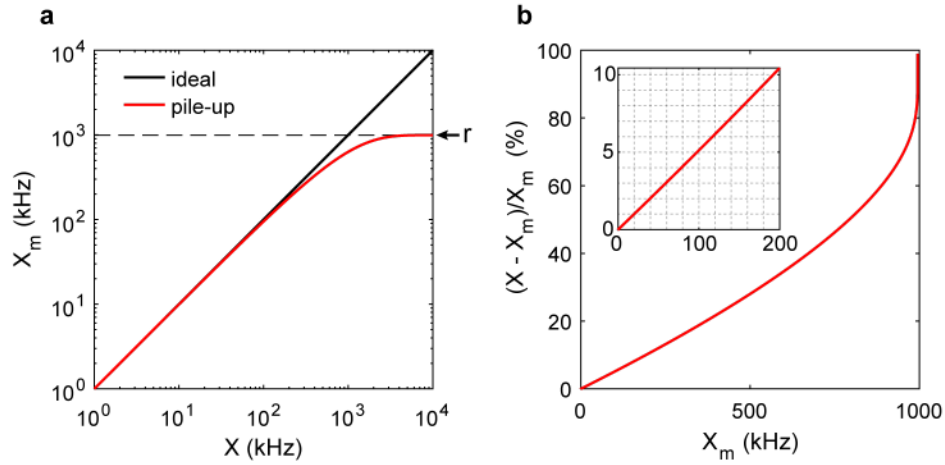

Figure S3: Model for pile-up error. (a) X vs X_m in the presence of pile-up (Eq. (S4), red) compared to the ideal case where every photon is registered (black), with r indicated (dashed black). (b) Percent error in X_m, with inset showing the 0 - 200 kHz range.

The repetition-rate of our excitation pulses is fixed at $r = 994.7$ kHz, while the fluorescence lifetime of the fluorophores used is typically on the order of a few nanoseconds. Therefore, essentially all useful signal light will arrive at the detector in the few first percent of the $\sim$1 μs duty cycle. Our detector has a hardware fixed dead-time of 75 ns, so that once a photon is detected any subsequent photons reaching the detector during this dead-time interval will not be registered. In practice this means that at most one photon can be counted per excitation pulse sequence, and the measured count rate will therefore saturate at the repetition-rate. However, even at lower count rates it is

possible that multiple signal photons will arrive at the detector per excitation cycle, only the first of which will be counted. The measured count rate will therefore always be smaller than the true count rate, with the error growing as the count rate approaches saturation. It is important to note that this possibility of multiple photons per pulse sequence is only relevant for the case of an ensemble of uncorrelated emitters, e.g. from a solution at concentrations greater than a few nM. If an individual molecule is being observed then only one photon can be emitted at a time anyways, and this type of pile-up is not an issue. In practice, however, this distinction is not important in our measurements because the single-molecule count rates we encounter are far below the pile-up threshold, as shown below.

As described in the main text, the total count rate is kept below a certain level to ensure that pile-up errors are small. To determine what this level should be, we consider a simple model where the probability of n photons reaching the detector after an excitation pulse sequence follows a Poisson distribution

$$p(n, \lambda) = \frac{e^{-\lambda}\lambda^n}{n!}. \tag{S1}$$

Here the rate parameter λ is the average photon number $\langle n \rangle$, and therefore the true count rate, i.e. without pile-up, is $X = r\lambda$ where r is the pulse repetition-rate. The measured count rate X_m is equal to the repetition-rate times the average number of photons counted per pulse sequence

$$X_m = r\langle n_c \rangle = r \sum_{n=0}^{\infty} n_c(n) p(n, \lambda), \tag{S2}$$

where the number of counted photons is

$$n_c(n) = \begin{cases} 0 & n = 0 \\ 1 & n \geq 1. \end{cases} \tag{S3}$$

Evaluating this expression, we get

$$X_m = r\Big(0 + \sum_{n=1}^{\infty} \frac{e^{-\lambda}\lambda^n}{n!}\Big) = r\Big(-e^{-\lambda} + \sum_{n=0}^{\infty} \frac{e^{-\lambda}\lambda^n}{n!}\Big) = r(1 - e^{-\lambda}) = r(1 - e^{-X/r}). \tag{S4}$$

This gives the relationship between the true count rate X and measured count rate X_m, which is inverted to give the correction function cited in the main text,

$$X = -r \ln(1 - X_m/r). \tag{S5}$$

Figure S3(a) shows the relationship between X and X_m for this model, while the corresponding magnitude of error in X_m is shown in Figure S3(b). For count rates below ~200 kHz, the error grows linearly in X_m with the approximate rate of 1% per 20 kHz. Beyond this range the growth rate increases and eventually diverges as saturation $X_m \sim r$ is approached.

To test how well Eq. (S5) works to correct real data, we measured the I_{vis}-dependence of the fluorescence count rate from a 1 μM Rhodamine 6G (R6G) solution in acetonitrile-d3. We used the same experimental configuration as an FEIR measurement (with a glass coverslip), although with the IR beam blocked. R6G is directly resonant with the visible pulse, and this concentration should be high enough to ensure we observe a large ensemble of molecules with low individual excitation probabilities to avoid photophysical saturation. Ideally, the true count rate should therefore be

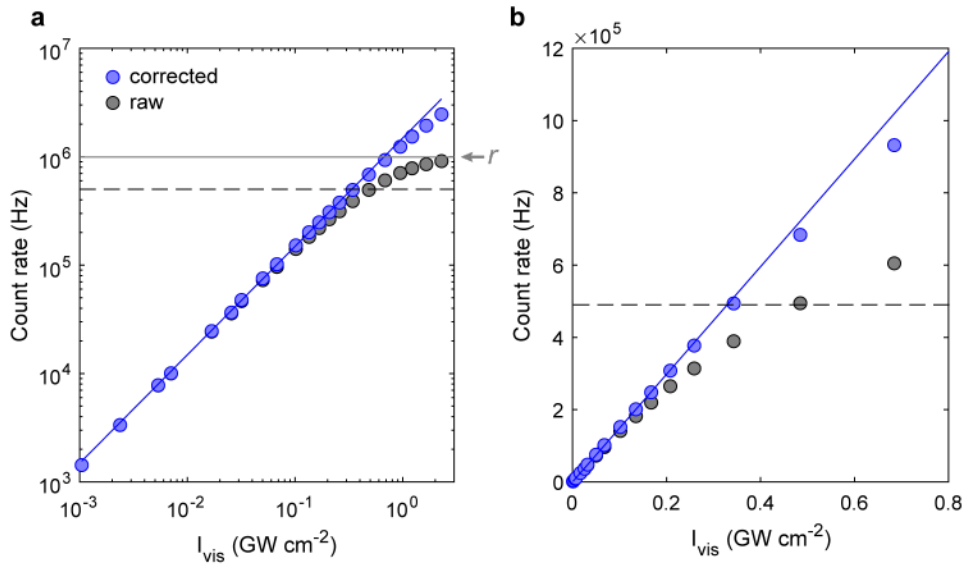

Figure S4: Testing the pile-up correction. Raw (black) and corrected (blue) count rates as a function of I_{vis} on log-log (a) and linear (b) axes (note the smaller I_{vis} range in (b)). The blue line is a linear fit to the corrected points with $I_{\mathrm{vis}} < 0.2$ GW cm^{-2}. The dashed line indicates 500 kHz, which we feel is the practical limit of measured count rate that can be successfully corrected.

linear in I_{vis}, and any deviations in the measured count rate reflect pile-up error. Figure S4 shows the raw and corrected count rates from this experiment on both log-log (panel (a)) and linear (panel (b)) axes. Applying the correction successfully restores a linear intensity dependence for measured count rates up to ∼500 kHz (dashed line). However, beyond this point the quality of the correction evidently breaks down, as the corrected points fall below the low-intensity linear trend (blue line). In this work we keep the measured count rate below 200 kHz (∼10% error before correction), which we feel is safely within the range that can be pile-up corrected with high fidelity by Eq. (S5).

S3 Complete coumarin series high concentration FEIR data and acquisition details

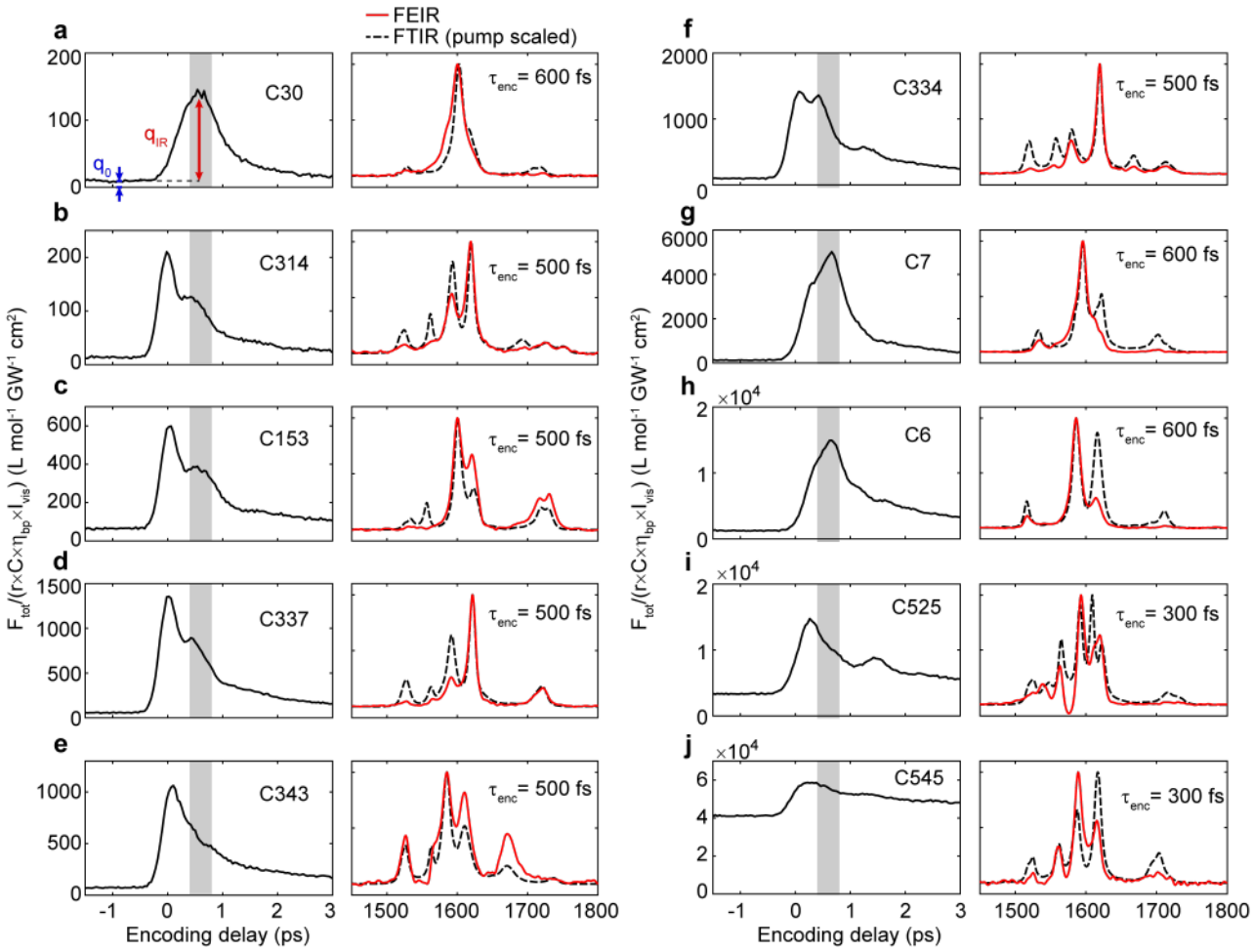

Figure S5: (a-j) Left panels: Total photon output F_{tot} from 2-pulse experiments on each coumarin plotted in brightness units. The effective FEIR (q_{IR}) and direct excitation (q_0) brightness are indicated by arrows in (a) and are found analogously for the remaining data. Right panels: Comparison of IR pump spectrum-scaled FTIR spectra (dashed line) with FEIR spectrum (solid line) at the encoding delay indicated.

Figure S5 shows the full series of FEIR measurements analogous to main text Figure 4 for all coumarins. The proper assignment of time zero for τ_{enc} (i.e. the center of the IR/Vis temporal intensity cross-correlation) is made difficult by the counter-propagating experimental geometry, which couples the relative timing of the IR and visible pulses to longitudinal position along the optical axis. In practice, this means that whatever sample or material is being used to characterize pulse overlap (using e.g. some non-linear process that produces a signal proportional to the product of IR and visible intensity profiles) must also have the same thickness and index profile as the sample the FEIR measurement is being performed on. For the FEIR experiments presented here, we have not yet found such a suitable "timing" sample, and instead assign $\tau_{\mathrm{enc}} = 0$ to be at the maximum of the earliest spike found in the 2-pulse transients for some of the coumarins (C314, C153, C337,

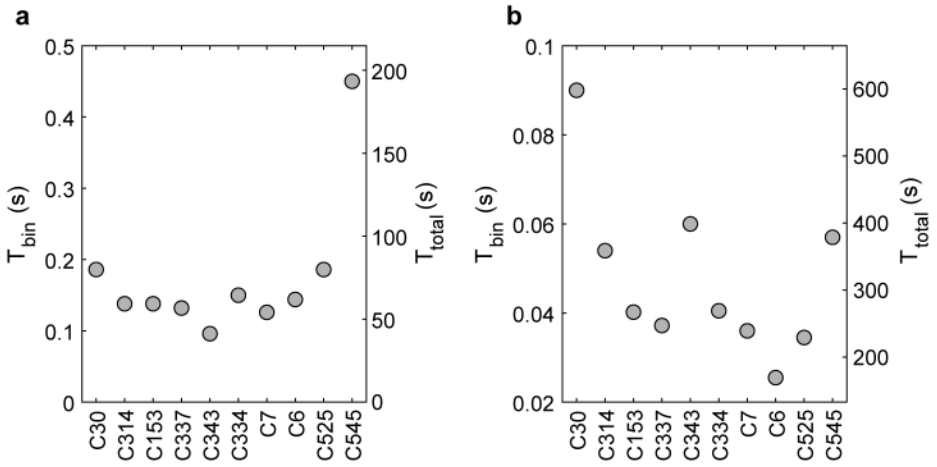

Figure S6: Integration time per bin (T_{bin}, left axis) and total experimental acquisition time (T_{total}, right axis) for (a) the 2-pulse transients and (b) spectra shown in Figure S5.

C343, C334). We believe it is likely that this spike has contributions from some of the pulse-overlap effects mentioned in the main text, which would justify our assignment of $\tau_{\text{enc}} = 0$. The relative timing of τ_{enc} between all the FEIR measurements is correct within an uncertainty of ∼100 fs.

The 2-pulse transients were recorded with 40 fs τ_{enc} bins from roughly -3 to 10 ps (323 total bins), while the τ_{IR} scan range used for the FT spectra (raw data not shown) was from -2 to 8 ps with 2 fs bins (4995 total bins). The continuous-scanning procedure used to sweep these delays as well as the processing steps for FT spectra have been described previously.[2, 3] In both cases, the scan speed of the delay stage was 2 mm/s (scan rates of ∼3 and ∼0.15 ms per bin, respectively), and photon counts were accumulated over many scans. To represent the data acquisition time in these measurements, Figure S6 shows the effective integration time per bin (T_{bin}), i.e. number of scans times scan rate per bin, for each measurement in Figure S5. The total data acquisition time of a measurement (T_{total}) is found by multiplying T_{bin} by the total bin number and constant factor of ∼1.33 which accounts for dead-time during stage turnaround and software latency.

S4 Instrument-dependent uncertainty in brightness values

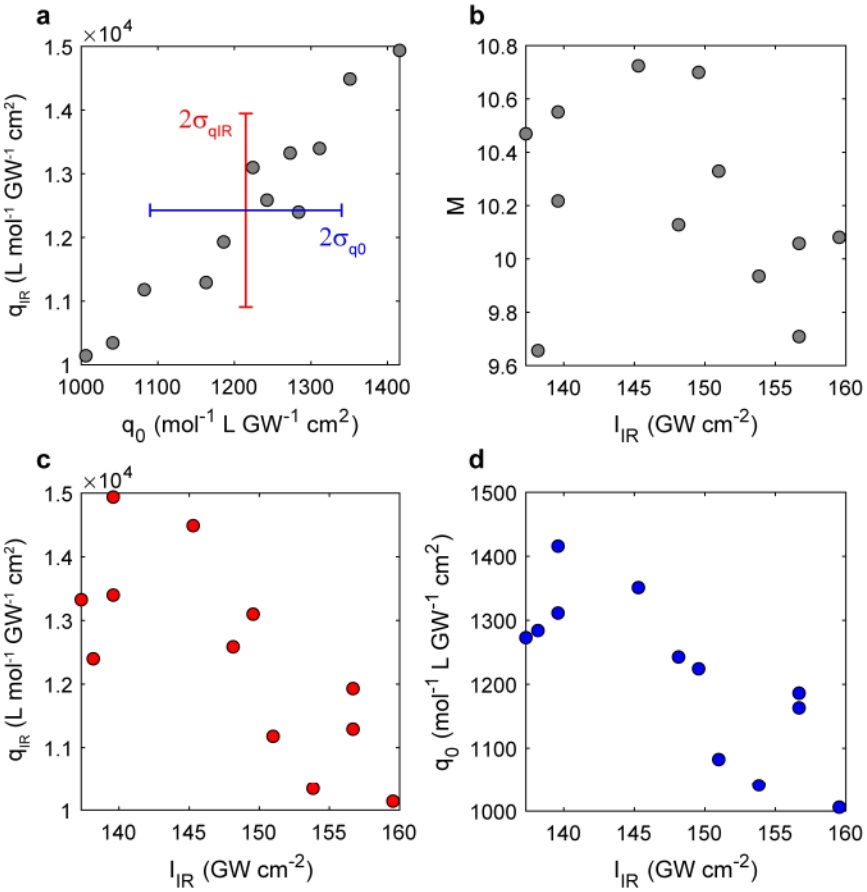

Figure S7: (a) q_{IR} vs. q_0 from repeat measurements on C6 ($\mu_{q_{\mathrm{IR}}} = 1.24 \times 10^4$ L mol^{-1} GW^{-1} cm^{-2}, $\sigma_{q_{\mathrm{IR}}} = 0.15 \times 10^4$ L mol^{-1} GW^{-1} cm^{-2}, $\mu_{q_0} = 1.22 \times 10^3$ L mol^{-1} GW^{-1} cm^{-2}, $\sigma_{q_0} = 0.13 \times 10^3$ L mol^{-1} GW^{-1} cm^{-2}). (b) M, (c) q_{IR}, and (d) q_0 vs. I_{IR} from the same set of measurements.

Estimating the error in the experimental FEIR and one-photon brigthnesses is difficult due to the many parameters used in their determination, as well as factors beyond direct control. Here we investigate the contribution from the most important of this latter category—day-to-day variations in IR intensity and the overall alignment of the instrument. Figure S7(a) shows the q_{IR} and q_0 values from 12 independent measurements on C6 each taken on separate days during the period when the data in main text Section IVC was collected. These measurements shared the same nominal experimental configuration include the use of glass coverslips. The vertical and horizontal bars indicate intervals of 2 standard deviations around the mean in q_{IR} and q_0, respectively. Notably, the variation in these values are highly correlated to each other as evident from the clustering along the diagonal. Figure S7(b) shows the corresponding modulation ratios against I_{IR} (calculated from the measured average IR power out of the OPA assuming a constant pulse duration, spot size, and transmission factor), which shows day-to-day variations with mean $\mu = 148$ GW cm^{-2} and standard deviation $\sigma = 8$ GW cm^{-2}. M does not appear to be correlated to I_{IR} over this range, which is at odds with the linear power dependence assumed in our model. As shown in Figures S7(c) and (d), both q_{IR} and q_0 are anti-correlated with I_{IR} over this range, which explains part of the spread and correlation in panel (a). As noted in main text Section IIB, these IR intensities are

near the upper limit that can be tolerated before thermal effects become severe, leading to more significant decreases in overall fluorescence collection efficiency and eventually bubble formation in the solvent. The negative trend in q_{IR} and q_0 in panels (c) and (d) is most likely a result of such a thermal effect, although of manageable severity. Because of this thermal effect, we will use the average value of I_{IR} when converting between q_{IR} and q. The remaining variation in q_{IR} and q_0 is likely due to the overall microscope alignment. Systematic errors in sample concentration were not characterized.

S5 Brightness vs. extinction on linear axes, FEIR brightness at signal maximum, and correlation incorporating $\varepsilon_{\mathrm{IR}}$

Table S1 lists the numerical values for three versions of the FEIR brightness (q, q_{IR}, and $q_{\mathrm{IR}}^{\mathrm{max}}$) and the one-photon background brightness q_0. As mentioned in the previous section, q is derived from q_{IR} by dividing out the average value of I_{IR} over all measurements in order to avoid including spurious variations due to thermal effects (present with glass coverslips). $q_{\mathrm{IR}}^{\mathrm{max}}$ is analogous to q_{IR} but uses the maximum value of F, regardless of the encoding delay at which it occurs. Figure S8 shows the same data as main text Figure 5(a), but on linear axes with q_{IR} vs. $\varepsilon_{\mathrm{el}}(\omega_{\mathrm{IR}}+\omega_{\mathrm{vis}})$ and q_0 vs. $\varepsilon_{\mathrm{el}}(\omega_{\mathrm{vis}})$ displayed on separate plots. The linear regressions were performed on this unmodified data, and the logarithmic scaling in the main text is merely to show the many decades in each axis.

Figure S9 compares the correlation between effective FEIR cross-section and $\varepsilon_{\mathrm{el}}(\omega_{\mathrm{IR}}+\omega_{\mathrm{vis}})$ using q as defined in the main text (averaging over $400 < \tau_{\mathrm{enc}} < 800$ fs) and alternately using the maxiumum signal, i.e. $q_{\mathrm{IR}}^{\mathrm{max}}/I_{\mathrm{IR}}$. Using the signal maximum produces a higher R^2 value and slightly higher slope. The inset in panel (b) shows the ratios of FEIR brightnesses calculated using the two methods. Panel (c) shows the M values using the maximum signal againt κ (cf. main text Figure 5b). The resulting correlation (correlation coefficient 0.69) is better than the case shown in the main text, but still diffuse.

Figure S10 shows the correlation between q/ϕ and the product of $\varepsilon_{\mathrm{el}}(\omega_{\mathrm{IR}}+\omega_{\mathrm{vis}})$ and $\varepsilon_{\mathrm{IR}}$ as defined by main text Eq. (15) and displayed for each coumarin in the inset to panel (a).

Table S1: FEIR and one-photon background brightnesses

Coumarin	q (L mol^{-1} GW^2 cm^{-4})	q_{IR}(L mol^{-1} GW cm^{-2})	$q_{\mathrm{IR}}^{\mathrm{max}}$ (L mol^{-1} GW cm^{-2})	q_0 (L mol^{-1} GW cm^{-2})
30	7.79×10^{-1}	1.24×10^{2}	1.36×10^{2}	9.80
314	5.89×10^{-1}	9.33×10^{1}	1.97×10^{2}	1.38×10^{1}
153	1.90	3.01×10^{2}	5.35×10^{2}	6.43×10^{1}
337	4.35	6.90×10^{2}	1.30×10^{3}	5.61×10^{1}
343	3.00	4.75×10^{2}	9.89×10^{2}	7.35×10^{1}
334	5.81	9.21×10^{2}	1.32×10^{3}	9.65×10^{1}
7	2.79×10^{1}	4.41×10^{3}	4.89×10^{3}	1.26×10^{2}
6	7.94×10^{1}	1.24×10^{4}	1.37×10^{4}	1.24×10^{3}
525	4.66×10^{1}	7.39×10^{3}	1.14×10^{4}	3.36×10^{3}
545	9.20×10^{1}	1.46×10^{4}	1.75×10^{4}	4.11×10^{4}

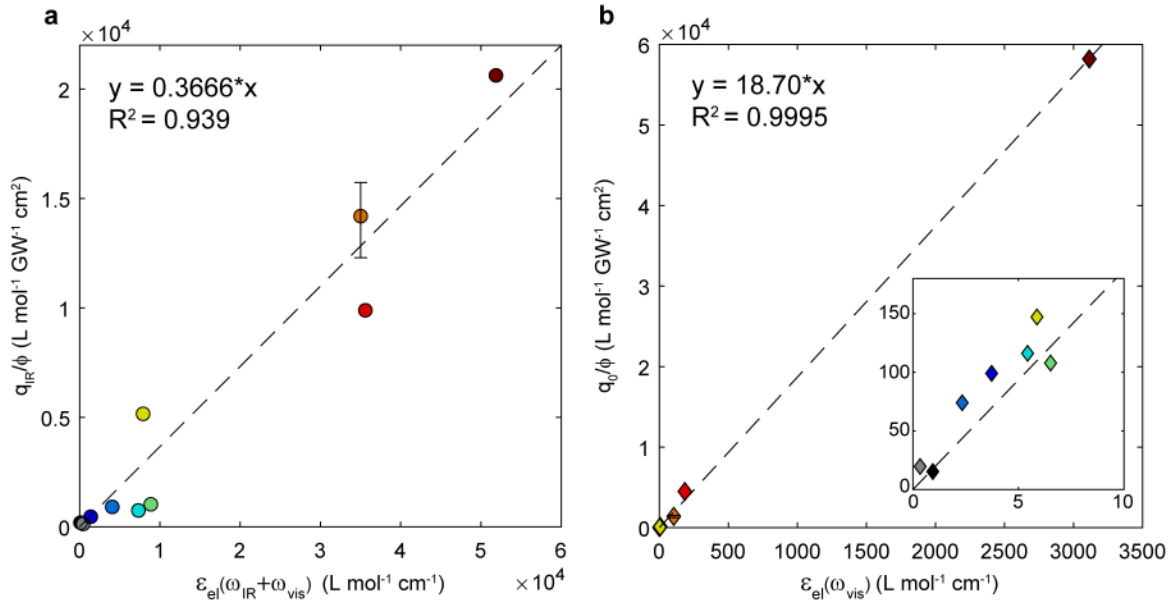

Figure S8: (a) q_{IR} vs. $\varepsilon_{\mathrm{el}}(\omega_{\mathrm{IR}}+\omega_{\mathrm{vis}})$ and (b) q_0 vs. $\varepsilon_{\mathrm{el}}(\omega_{\mathrm{vis}})$ on linear axes. These data and the linear regressions (dashed lines) are the same as shown main text Figure 5a. The vertical error bars for C6 indicate a range of 2 standard deviations from experimental uncertainty referred to in the main text and described in the previous section. The inset in (b) shows a blown up view of the points near the origin.

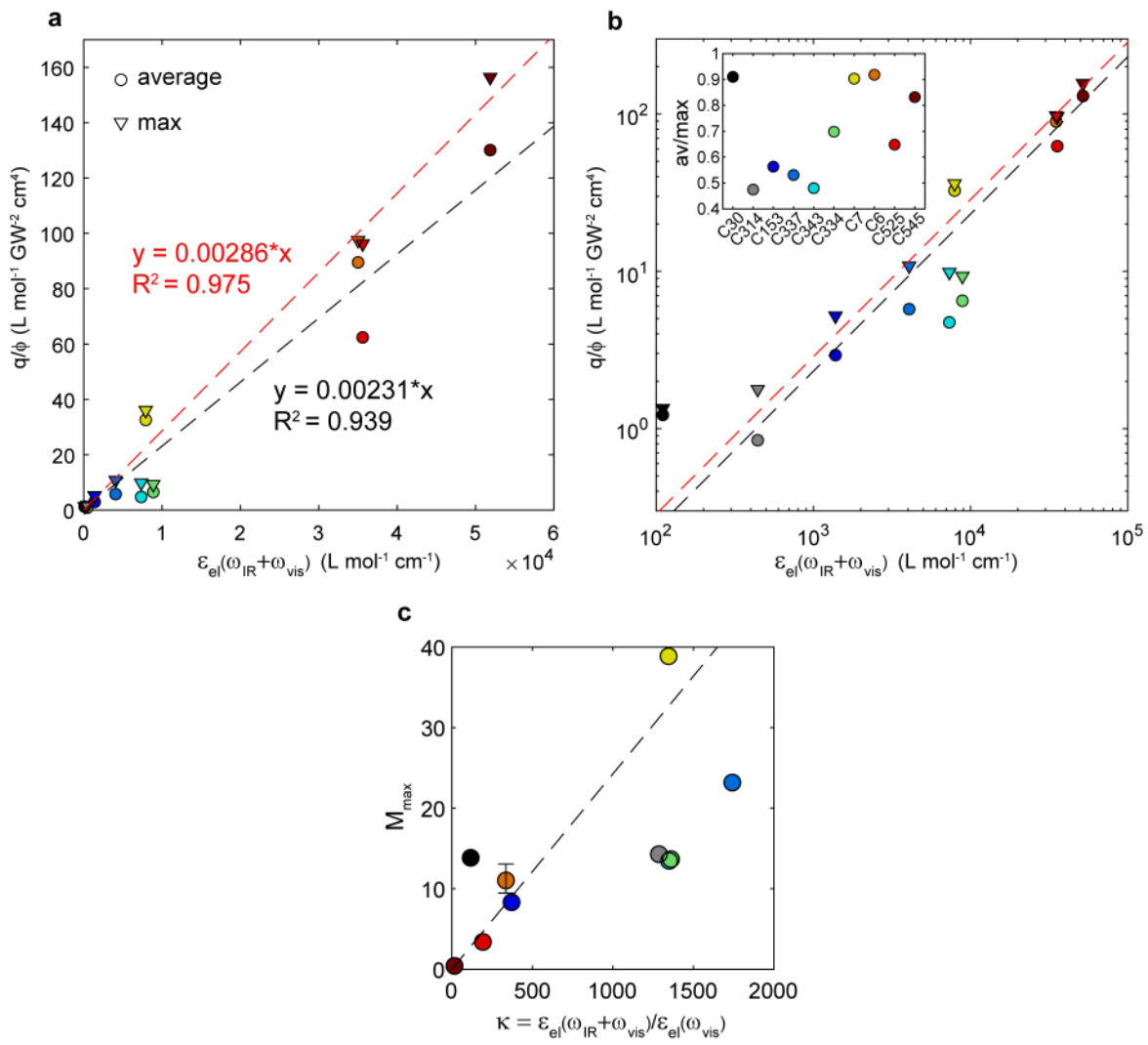

Figure S9: Effect on the q/ϕ vs. $\varepsilon_{\mathrm{el}}(\omega_{\mathrm{IR}} + \omega_{\mathrm{vis}})$ correlation when alternately using the signal maximum (triangles, regression line in red) instead of the averaged signal as in the main text (circles, regression line in black). (a) linear axes and (b) log-log axes. Ratios of FEIR brightness from the averaged signal to max signal (insert). (c) M using the signal maxima vs. κ, with dashed line showing the quotient of the (red) linear regression slope with the q_0 vs. $\varepsilon_{\mathrm{el}}(\omega_{\mathrm{vis}})$ slope.

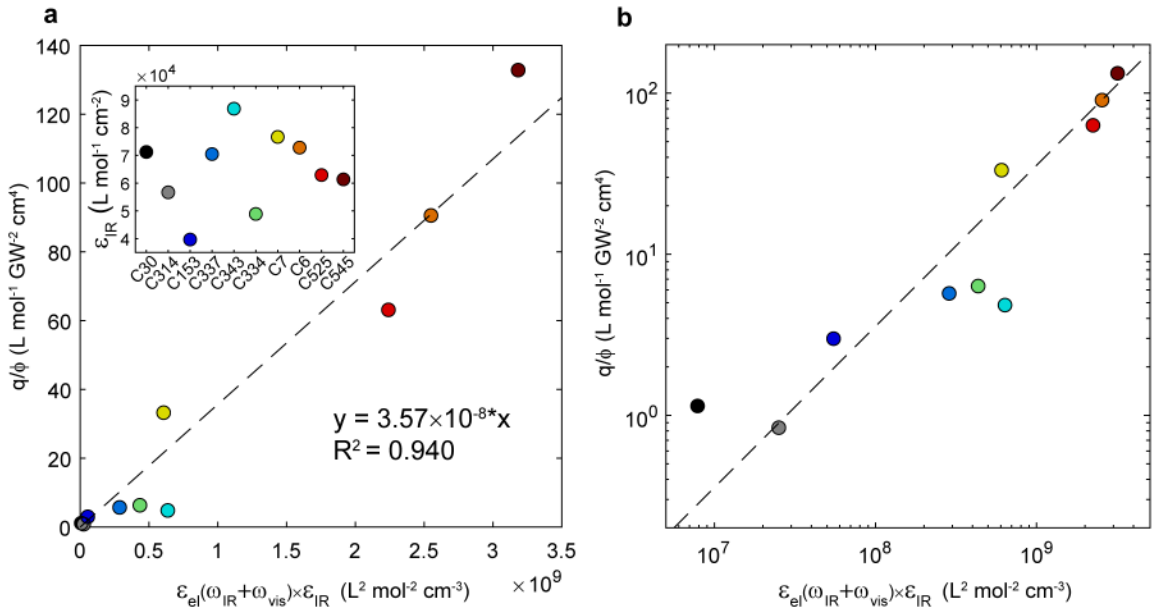

Figure S10: q/ϕ vs. $\varepsilon_{\mathrm{IR}} \times \varepsilon_{\mathrm{el}}(\omega_{\mathrm{IR}} + \omega_{\mathrm{vis}})$ on (a) linear and (b) log-log axes. Linear regressions indicated by dashed lines. The inset in (a) shows the $\varepsilon_{\mathrm{IR}}$ value for each coumarin.

S6 C6 and C7 concentration and visible intensity dependent data

Figures S11 and S12 show the full concentration and I_{vis} dependent FEIR data used in main text Section IVD. The raw count rate F_{tot}, background subtracted F count rate, and normalized F signal are shown for each concentration and intensity. The IR intensity is nominally constant, but varies day-to-day with a similar spread as discussed in Section S4. These measurements used CaF_2 coverslips. For all but 1 nM C7, 2 repeated measurements for each concentration and I_{vis} point were made and both are shown. The F count rate used in main text Figures 6 and 7 is the mean over $400 < \tau_{\mathrm{enc}} < 800$ fs averaged over the repeat measurements, while the background $F_0 + B$ is determined from the mean over $-3 < \tau_{\mathrm{enc}} < -1$ ps. In each case the error bars represent 2 standard deviations. For the measurements that exhibit saturation in I_{vis}, there is a small change in the shape of the decay transient (most apparent in the normalized signals) consistent with the suppression of the maximum, however the effect is subtle. The integration time per bin and total experimental acquisition times are summarized in Figure S13.

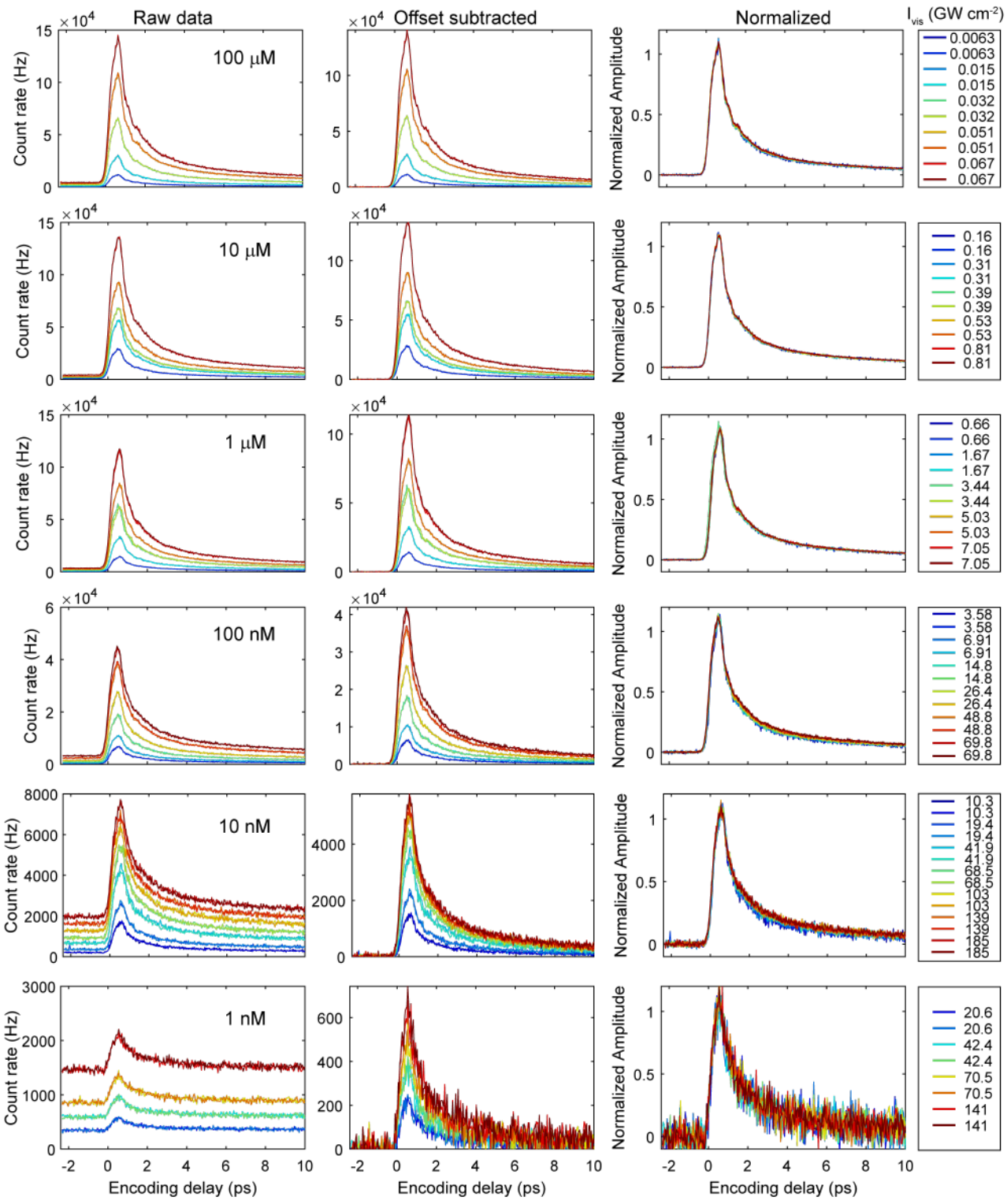

Figure S11: C6 concentration and I_{vis} dependent 2-pulse FEIR data.

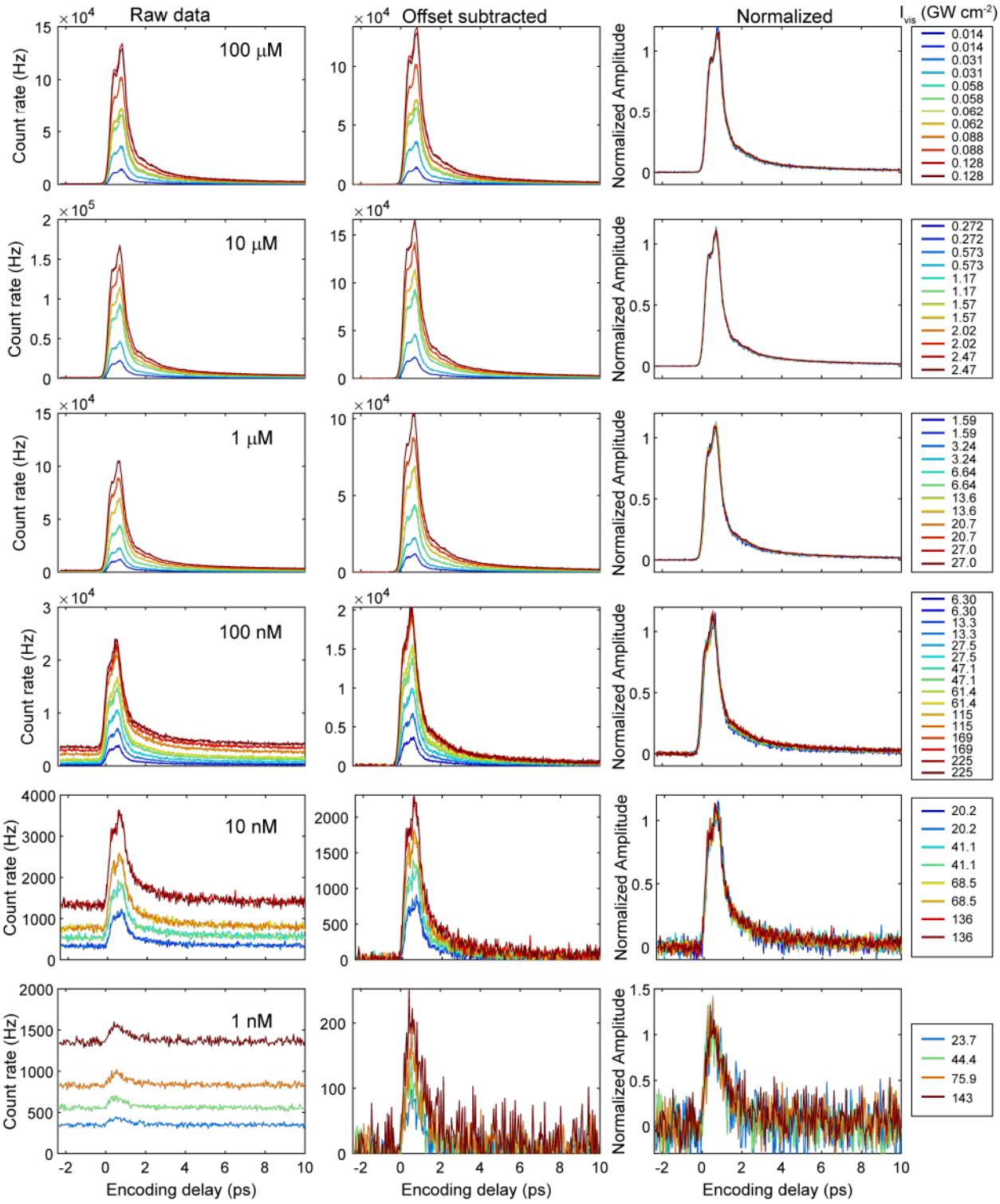

Figure S12: C7 concentration and I_{vis} dependent 2-pulse FEIR data.

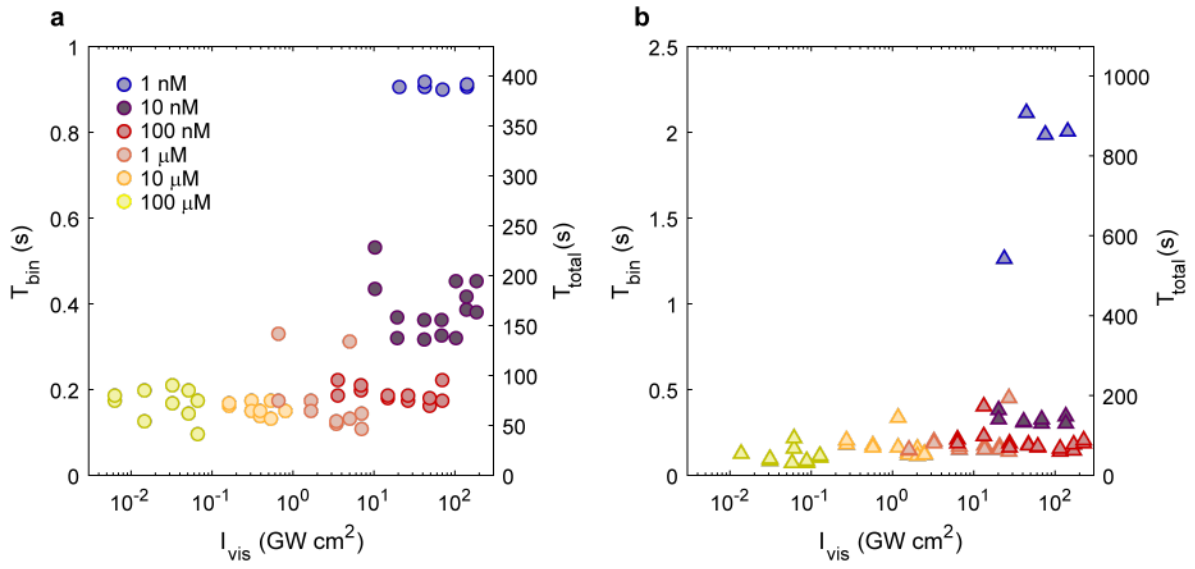

Figure S13: Integration time per bin (T_{bin}, left axis) and total experimental acquisition time (T_{total}, right axis) for the measurements on (a) C6 and (b) C7.

S7 Limiting concentrations of the coumarin series

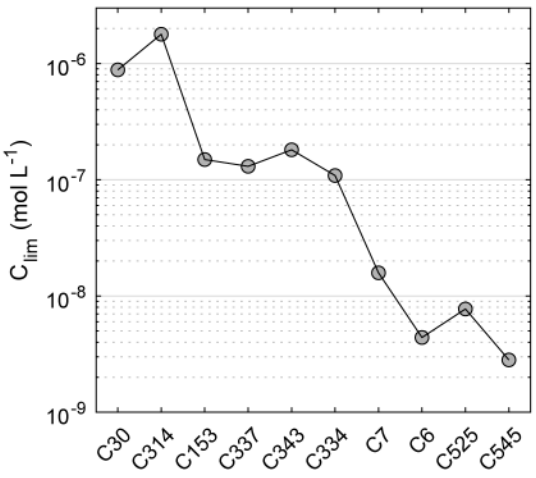

Figure S14: C_{lim} (main text Eq. (19)) for the coumarin series, using the q_{IR} values measured with glass coverslips (Table S1). The C_{lim} values for the newer sample configuration using CaF_2 coverslips are ~3 times lower.

S8 Details of encoding transition saturation behavior

The saturation curves for C6 and C7 shown in main text Figure 7 are reproduced here in Figure S15(a) and shown on log-log axes in Figure S15(b). We have also included a fit to the hyperbolic model (main text Eq. 20) which qualitatively follows the shape of the saturation curves slightly better than the exponential model. In the short pulse limit, saturation due to trapping in μs-lifetime triplet states is predicted to produce a hyperbolic shape to the saturation curve.[4] The I_{vis} dependence of the background level is shown in Figure S15(c) and (d) for C6 and C7, respectively. The constant dark count level $d = 43$ Hz has been subtracted off. Due to the concentration-independent B contribution, dividing the count rates by concentration as in panels (a) and (b) would not collapse the data onto a single trend (this is evident by the diminishing vertical offsets between the trends for each concentration as the concentration decreases). Data for each concentration is fit to a power law, and the resulting exponents are shown in Figure S15(e) and (f). These exponents are close enough to 1 to indicate an approximately linear intensity-dependence, although there is a slight decrease in exponent for the lowest concentrations where the highest I_{vis} are used.

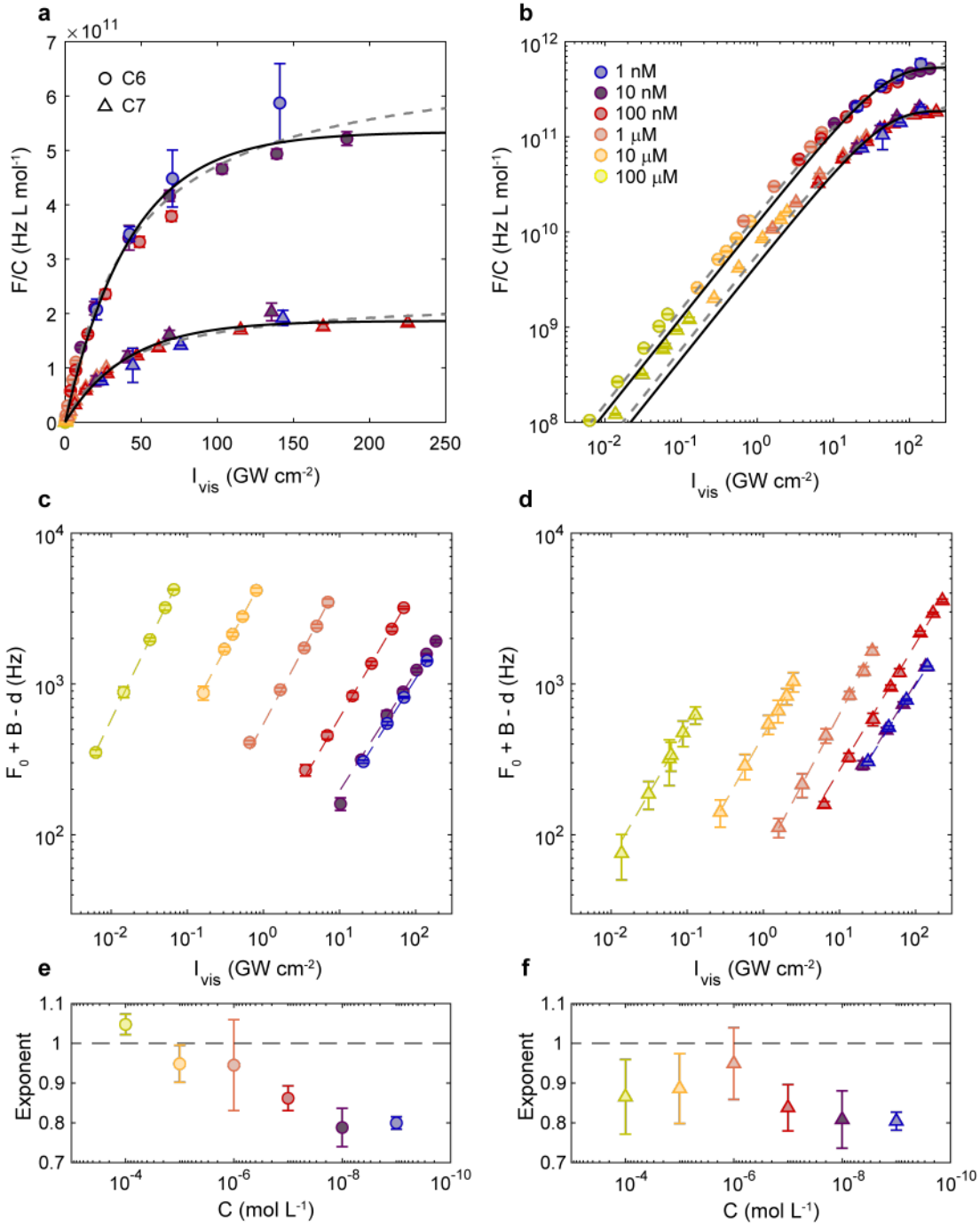

Figure S15: (a) F saturation curves for C6 (circles) and C7 (triangles). (b) same data as (a) on log-log axes. Fits to the exponential and hyperbolic models are shown by solid black and dashed gray lines, respectively. (c-d) Dark count subtracted background level vs. I_{vis} for C6 and C7, respectively. The color coding for concentration is the same as in (a) and (b). Power law fits for each concentration are shown by dashed lines. (e-f) Power law exponents from the fits in (c) and (d), respectively, with error bars indicating 95% confidence intervals.

S9 Visible intensity dependence for C30 and C314

Figure S16 summarizes the I_{vis} dependence for the two most pre-resonant coumarins in the series: C30 and C314. As mentioned in the main text, the background level is super-linear above a certain range, where it follows a quadratic I_{vis} dependence. The I_{vis} used for the brightness analysis are indicated by arrows in panels (b) and (e), and fall below the onset of this quadratic behavior. The F count rate also shows an apparent saturation behavior in I_{vis}, and the saturation thresholds I_S extracted from fits to the exponential model in discussed in main text Section IVD are listed. However, as the concentration is high (100 μM for both), the measured count rates correspond to very small overall excitation probabilities, so this mechanism for the observed saturation is unlikely. Given the deeply pre-resonant excitation conditions and the corresponding cross-over to multiphoton background excitation, a different explanation beyond our current treatment of the FEIR excitation process is likely needed to explain this effect.

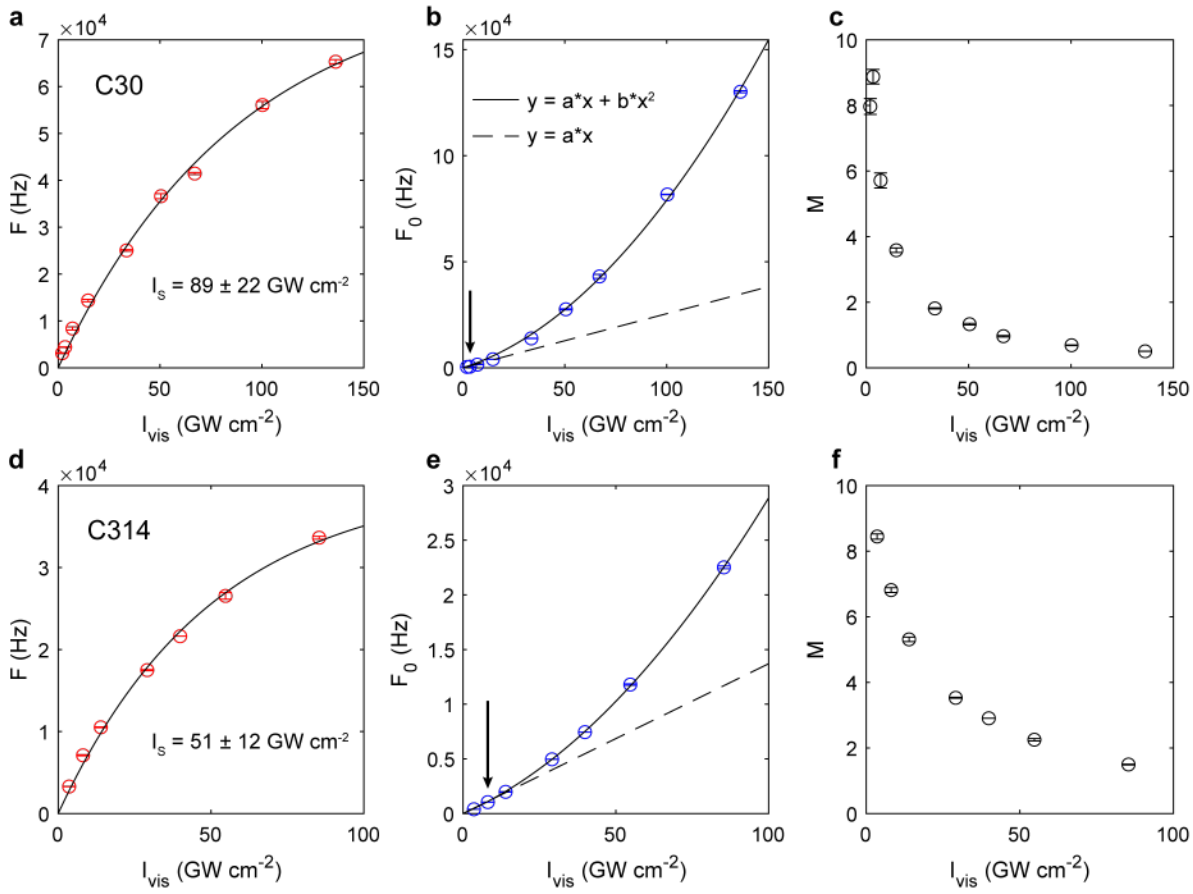

Figure S16: I_{vis}-dependence of (a) F, (b) F_0, and (c) M for C30. Panels (d-f) show the analogous information for C314. Fits to the exponential saturation model are shown as black lines in (a) and (d) with corresponding I_S listed. (b) and (e) include fits to a quadratic polynomial (solid line) and linear dependence of the first 3 points (dashed line), while the black arrows indicate the I_{vis} used in the brightness analysis.

S10 FEIR-CS on 1 nM C6 solution

The FEIR-CS measurement used to determine $\langle N \rangle$ for the 1 nM C6 solution is shown in Figure S17. A CaF_2 coverslip was used. Details on the method and procedure are found in Ref. [3]. $\langle N \rangle$ is given by the inverse of the early-time amplitude $G(0)$ of the correlation function, which is extracted from a fit to the data using a standard model assuming diffusion through a Gaussian probe volume.[3]

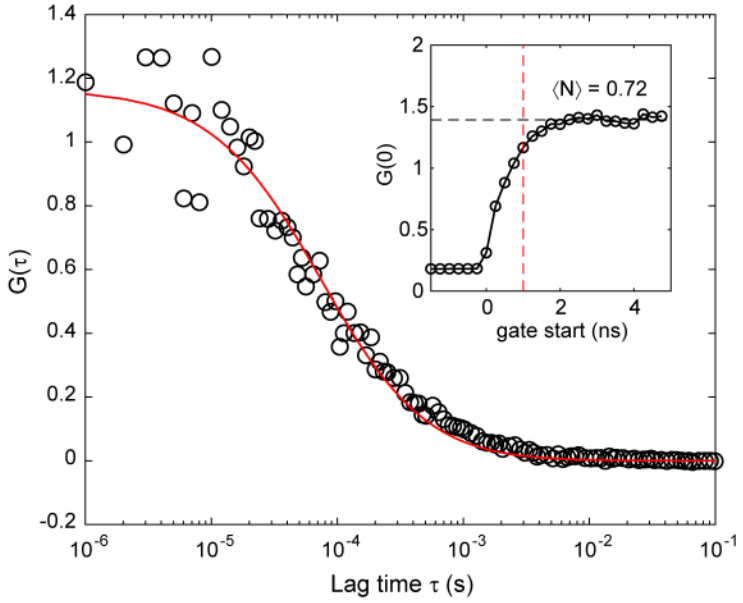

Figure S17: FEIR-CS data on the 1 nM C6 solution at $I_{vis} = 42$ GW cm^{-2} (black circles) with fit to a standard diffusion model (red). The inset shows the dependence on the early time amplitude $G(0)$ extracted from the fit on the starting edge of the time-gate used to filter the photon stream, with the limiting value of 1.39 (corresponding to $\langle N \rangle = 0.72$) indicated. The red dashed line indicates the 1 ns starting edge of the time-gate used for the data in the main plot.

References

(1) Arlt, J.; Tyndall, D.; Rae, B. R.; Li, D. D.-U.; Richardson, J. A.; Henderson, R. K. A study of pile-up in integrated time-correlated single photon counting systems. *Rev. Sci. Instr.* **2013**, *84*, 103105, DOI: 10.1063/1.4824196.

(2) Whaley-Mayda, L.; Penwell, S. B.; Tokmakoff, A. Fluorescence-Encoded Infrared Spectroscopy: Ultrafast Vibrational Spectroscopy on Small Ensembles of Molecules in Solution. *J. Phys. Chem. Lett.* **2019**, *10*, 1967–1972, DOI: 10.1021/acs.jpclett.9b00748.

(3) Whaley-Mayda, L.; Guha, A.; Penwell, S. B.; Tokmakoff, A. Fluorescence-Encoded Infrared Vibrational Spectroscopy with Single-Molecule Sensitivity. *J. Am. Chem. Soc.* **2021**, *143*, 56, DOI: 10.1021/jacs.1c00542.

(4) Humpolíčková, J.; Benda, A.; Enderlein, J. Optical Saturation as a Versatile Tool to Enhance Resolution in Confocal Microscopy. *Biophys. J.* **2009**, *97*, 2623–2629, DOI: https://doi.org/10.1016/j.bpj.2009.08.002.